Automating the Hartman-Schijve Methodology for Predicting Interlaminar Fatigue Crack Growth in Fibre Composites

Ramesh Chandwani[1], Chris Timbrell[1*], Bamber R.K. Blackman[2], Rhys Jones[3] and Anthony J. Kinloch[2]

[1]Zentech International Limited, 590B Finchley Road, London, NW11 7RX, UK.
[2]Department of Mechanical Engineering, Imperial, Exhibition Road, London, SW7 2AZ, UK.
[3]Department of Mechanical and Aerospace Engineering, Monash University, Clayton, Victoria, 3800, Australia.

Abstract:
The Hartman-Schijve methodology offers a direct route to calculating various fatigue crack growth (FCG) rate curves that are associated with delaminations growing in fibre polymer-matrix composites. However, up to the present, only a 'manual' method has been described to deduce the values of the Hartman-Schijve constants that are needed for such calculations. Whilst this manual method may give reasonably acceptable results for calculating the Hartman-Schijve constants, it is a difficult and tedious implementation route. Thus, it may, if the operator is inexperienced, give relatively large errors in the values of the key constants that are needed to calculate the FCG rate curves. Furthermore, for very large data sets there is great difficulty incurred in manipulating such a large amount of data using the 'manual method'.

Therefore, the main aim of the present paper has been to introduce a novel computer model and the associated software, 'Zencrack : Material Curve Fitting Utility' from Zentech International Limited, UK, to obtain automatically the Hartman-Schijve constants. The aim has been to deduce the 'worst-case upper-bound' FCG curve for small, naturally-occurring, delaminations in the composite material, or component. To achieve such an 'automatic' method, the current work (a) has taken previously-published algorithms that employ a 'Total Least Squares' method for the fitting process of the experimental input data to the Hartman-Schijve equation and (b) has investigated the effect of a normalising scaling factor. It is shown that an automatic calculation that includes all the input data gives the best representation of the Hartman-Schijve constants and is the recommended approach.

Keywords: automating fatigue predictions, carbon-fibre composites, fatigue, total least squares method

*Corresponding author: Chris Timbrell (chris.timbrell@zentech.co.uk)

NOMENCLATURE

a	total crack (delamination) length, measured from the loading line
a_o	length of the initial delamination in the DCB test specimen, i.e. the length of the (thin) film used as a starter crack, measured from the loading line
a_p	length of the pre-crack (i.e. pre-delamination), measured from the loading line, in the DCB test specimen prior to cyclic-fatigue fracture measurements being taken
a_p-a_o	pre-crack (i.e. pre-delamination) extension length in the DCB test specimen prior to cyclic-fatigue fracture measurements being undertaken
A	apparent cyclic fracture toughness
AGS	a numerical algorithm, using minimization of multiextremal functions under nonconvex constraints
CFRP	carbon-fibre reinforced-plastic
CGROW	an existing software providing a framework for the determination of fatigue crack growth model parameters
CSAM	cold spray additive-manufacturing
CUHYSO	a numerical algorithm, the acronym expanding to Contracting Uniform Hyper-Rectangles Sampling for Optimization
da/dN	fatigue crack (i.e. delamination) growth (FCG) per cycle
D	value of da/dN as the intercept in the Hartman-Schijve crack-growth equation using a double-logarithmic plot
DADT	durability and damage tolerance
DCB	double cantilever beam
FCG	fatigue crack growth
G	energy release-rate
G_{co}	quasi-static value of the Mode I (tensile) interlaminar fracture energy at the onset of crack growth as determined from [1]
G_{max}	maximum value of the applied energy release-rate in the fatigue cycle
G_{min}	minimum value of the applied energy release-rate in the fatigue cycle
ΔG	range of the applied energy release-rate in the fatigue cycle, as defined below $= G_{max} - G_{min}$
$\Delta\sqrt{G}$	range of the applied energy release-rate in the fatigue cycle, as defined below $= \sqrt{G_{max}} - \sqrt{G_{min}}$
$\Delta\sqrt{G_{thr}}$	range of the fatigue threshold value of $\Delta\sqrt{G}$, as defined below $= \sqrt{G_{max.thr}} - \sqrt{G_{min.thr}}$
K	stress-intensity factor
ΔK	range of the stress-intensity factor in a fatigue cycle
ΔK_{thr}	range of the fatigue threshold value of ΔK, as defined below $= K_{max.thr} - K_{min.thr}$
LEFM	linear-elastic fracture-mechanics
MLSL LDS	a numerical algorithm, the acronym expanding to Multi-level Single-Linkage with Sobol Low-Discrepancy sequence
n	exponent in the Hartman-Schijve crack-growth equation using a double-logarithmic plot
N	number of fatigue cycles
NASA	North American Space Administration
NASGRO	a suite of software programs used to analyse fatigue in structures
P_{max}	maximum load applied during the fatigue test
P_{min}	minimum load applied during the fatigue test

R	R-ratio (=P_{min}/P_{max})
R^2	coefficient of determination
s	scaling parameter
USA	United States America
USAF	United States Airforce
$\Delta\kappa$	crack driving force, i.e. the similitude parameter, sometimes referred to as the Schwalbe parameter
σ	standard deviation

1. Introduction

The design of composite airframes, based on continuous carbon-fibres in an epoxy thermosetting polymeric matrix, under cyclic fatigue loadings typically follows one of two main philosophies: the 'no-growth' approach or the 'slow-growth' approach [2]. Although the no-growth of a crack, i.e. delamination, strategy is the most commonly implemented, it is widely recognised that this method can lead to overly conservative structures. Moreover, studies [3,4] have demonstrated that even in designs intended to prevent crack propagation, delaminations can still initiate and grow during operational service. Consequently, a key issue currently facing engineers and researchers in the composites field is how to evolve the no-growth philosophy to allow for the initiation and limited progression of small, naturally-occurring, delaminations. This evolution calls for the development of analytical and computational tools capable of evaluating the structural integrity of composite airframes that may contain such small delaminations subjected to realistic multi-axial flight loads. Importantly, to be consistent with the airworthiness standards delineated in the US Joint Services Structural Guidelines JSSG2006 [5] and MIL-STD-1530D [6], any growth that does occur should remain gradual and predictable. Furthermore, in accordance with [5-7] delaminations present in the structure must therefore undergo a thorough durability and damage tolerance (DADT) assessment [5,6]. As explained in MIL-STD-1530D, such assessments are best done using linear-elastic fracture-mechanics (LEFM).

The use of LEFM to perform the mandated durability assessment of delamination damage in a composite airframe subjected to realistic multi-axial flight loads relies on a prior knowledge of the relationship between the fatigue crack growth (FCG) rate, *da/dN*, per cycle and the energy-release rate, G. It is now well established [8-15] that the most appropriate approach for composite materials, such as a continuous carbon-fibre reinforced-plastic (CFRP), is to express *da/dN* as a function of the range of the applied energy release-rate, $\Delta\sqrt{G}$, in the fatigue cycle, as defined by $\Delta\sqrt{G} = \sqrt{G_{max}} - \sqrt{G_{min}}$; where G_{max} and G_{min} are the maximum and minimum values of the applied energy release-rate in the fatigue cycle, respectively. It

should also be noted that the NASA Fracture Design Handbook NASA-HDBK-5010 [7] mandates the use of a 'worst-case upper-bound' FCG rate curve for design and service-life studies. This 'worst-case upper-bound' FCG rate curve should encompass, and bound, all the experimental results and allow for scatter in the test data. A similar requirement is inherent in the United States Air Force Structures Bulletin EZ-SB-19-01 [16] which presents the certification guidelines for additively-manufactured aircraft parts. Thus, a methodology is needed for estimating the 'worst-case upper-bound' FCG rate curve from the laboratory test results that (a) that encompasses all the experimental data, (b) provides a conservative FCG curve which accounts for any retardation effects and (c) accounts for the experimental scatter that is frequently seen under fatigue loading. Such a FCG curve can then employed for developing, characterising and comparing different composite materials, and for designing and lifing in-service aircraft components and structures, using a 'slow growth' approach.

As discussed below, the Hartman-Schijve [17] methodology offers a direct route to calculating this 'worst-case upper-bound' FCG rate curve for small, naturally-occurring, delaminations. However, up to the present, only a 'manual' method has been described [e.g. 11-15], to implement this Hartman-Schijve method, although more recently this has been combined with a 'Total Least Squares' approach developed in [18]. Whilst the manual method may give a reasonably acceptable result, it is a difficult and tedious implementation route and may, if the operator is inexperienced, give relatively large errors in the values of the key parameters that are needed to calculate the 'worst-case' FCG rate curve. Furthermore, for very large data sets there is great difficulty incurred in manipulating such a large amount of data using a manual method. Therefore, the main aim of the present paper is to introduce a novel computer model, and the associated software, to obtain automatically the 'worst-case upper-bound' FCG rate curve for small, naturally-occurring, delaminations.

It should be noted that the present approach presents a somewhat different methodology to other computational tools, such as to be found for example in [19,20]. In these papers the main aims were somewhat similar, i.e. to develop a robust and efficient computational tool to simulate fatigue-driven delamination in complex composite structures. However, the approach in these papers was to exploit the peculiarities, in terms of mesh and load-step size independency of the well-established SMart–time XB procedure, based on the Virtual Crack Closure Technique approach, to develop a Paris Law-based module to mimic the delamination growth rate due to cyclic loads. The procedure in [19,20] takes advantage of the solver of the commercial finite element code 'Ansys Mechanical' and is fully implemented in the 'Ansys Parametric Design Language'. The implemented fatigue block interacts with the already existing modules, thus simulating the fatigue-driven delamination without mesh dependency and potentially accounting for the R-curve behaviour of the material. In contrast, the aim of the

present paper, as stated above, is to introduce a novel computer model, and the associated software (i.e. 'Zencrack : Material Curve Fitting Utility' from Zentech International Limited, UK) to obtain automatically the 'worst-case upper-bound' FCG rate curve for small, naturally-occurring, delaminations.

Thus, the present paper discusses in Section 2 the materials and experimental methods employed, and then in Section 3 the general form of the FCG rate curves that are measured. Next, in Section 4, the Hartman-Schijve modification of the NASGRO crack growth model that may be used to obtain this 'worst-case' FCG rate curve is introduced. To set the scene for the novel computational analyses to be described in the present paper, the implementation of the Hartman-Schijve methodology by a 'manual' approach is then outlined in Section 5. The major contribution of the present paper is the automatic implementation of the Hartman-Schijve methodology which is then discussed in depth, see Section 6. The main conclusions that may be drawn are then stated in Section 7.

2. Materials and Experimental Details

In the present paper we shall analyse FCG rate curves which have been published [mainly in 14,15] for a CFRP material which was fabricated using a prepreg of unidirectional, continuous carbon-fibres in a thermosetting epoxy polymer matrix ('M30SC/DT120' supplied by Delta-Tech S.p.A., Italy). Panels of CFRP were produced of this composite and were manufactured using a hand lay-up by the Delft University of Technology, the Netherlands, mainly with a unidirectional lay-up sequence. (A unidirectional, continuous carbon-fibre composite was chosen since this is the orientation of the fibres given in the ISO Standard test method [1] and this fibre orientation typically results in the most severe degree of fibre-bridging occurring.) In all cases, a 12.7 μm thick film of poly(tetrafluoroethylene) ('Teflon', Du Pont, Wilmington, DE, USA) was inserted into the mid-plane of the CFRP panel at one end, normal to the 0° fibre direction, during the hand lay-up process to act as an initial delamination, or 'starter crack', of a nominal length, a_o, of 50 mm. The laid-up panels were placed in an autoclave and cured for 90 minutes at a temperature of 120 °C under a pressure of 6 bar. The glass transition temperature of the resulting thermosetting epoxy polymer matrix was 120 °C. The panels were cut into strips to make double-cantilever beam (DCB) specimens [1] with an embedded starter crack in their mid-plane.

The testing procedure followed the approach outlined in more detail in [14,15] and was undertaken using a servo-hydraulic fatigue test machine equipped with a travelling microscope to measure the crack length. Initially, a crack was propagated under quasi-static loading from the starter crack (i.e. delamination) embedded in the DCB test specimen until a clearly visible and stable crack extension occurred, typically not exceeding 3.0 mm from the original starter

front, denoted as a_o. This extension, referred to as a_p-a_o served as the pre-crack length. (It should be noted that, if a pre-crack extension length of a_p-a_o is not used in the fracture mechanics test, then optimistically high values of the quasi-static toughness and fatigue resistance will be measured. This is because the starter crack film of length a_o represents a relatively blunt crack tip compared to that of a pre-crack of length a_p, which is naturally-grown ahead of the starter film prior to the commencement of the test.) For any given DCB specimen, the test method that was employed involved growing the crack under cyclic-fatigue loading, at a relatively low frequency of 5 Hz to avoid heating effects, for a relatively short distance from the initial value of the pre-crack extension length, a_p-a_o, whilst taking readings of the number of cycles, N, crack length, a, load, P, and displacement, δ. Fatigue cycling was initiated under displacement control, using a deformation range where the peak deformation matched the maximum experienced during the prior quasi-static phase. As a result, the DCB fatigue test began with a relatively high FCG rate of around 10^{-5} m/cycle and continued until much lower rates, of approximately 5 x 10^{-10} m/cycle, were observed. The fatigue test was then paused and restarted, this time using the newly-extended crack length, i.e. the new value of a_p-a_o, as the starting point for a subsequent FCG test. The value of the R-ratio used was typically 0.1, where R=P_{min}/P_{max}. The measured data were employed to calculate, for a given DCB test at a given value of the crack extension length, a_p-a_o, the FCG rate, da/dN, using the 'incremental polynomial method' [14,15,21]. Also, the values of the maximum and minimum energy release-rate, G_{max} and G_{min}, applied in a fatigue cycle were deduced from the maximum and minimum applied measured loads, P_{max} and P_{min}, respectively, using the 'modified compliance method' as described in detail in the ISO Standard [1].

3. The FCG Rate Curves

As previously reported [9-15], and exemplified in Figure 1, the FCG rate curves, plotted as logarithmic da/dN versus logarithmic $\Delta\sqrt{G}$, typically consistently shift to the right with increasing values of a_p-a_o; where $\Delta\sqrt{G} = \sqrt{G_{max}} - \sqrt{G_{min}}$. Thus, each new pre-crack length led to a distinct FCG rate curve until relatively high values of a_p-a_o were attained. This shift indicates a reduction in the FCG rate for a given $\Delta\sqrt{G}$ as the pre-crack length, a_p-a_o, increases, i.e. the crack propagates more slowly at higher a_p-a_o values. This trend is attributed to the increasing influence of fibre bridging within the DCB specimen. A longer pre-crack extension, a_p-a_o, facilitates more extensive fibre bridging, which acts to retard crack growth for a given energy-release rate. However, as illustrated in Figure 1 some degree of variability is inherent in the DCB test results, and this general pattern may not always be precisely followed [11-15], indicating that some scatter does, of course, exist in the measured FCG rate curves.

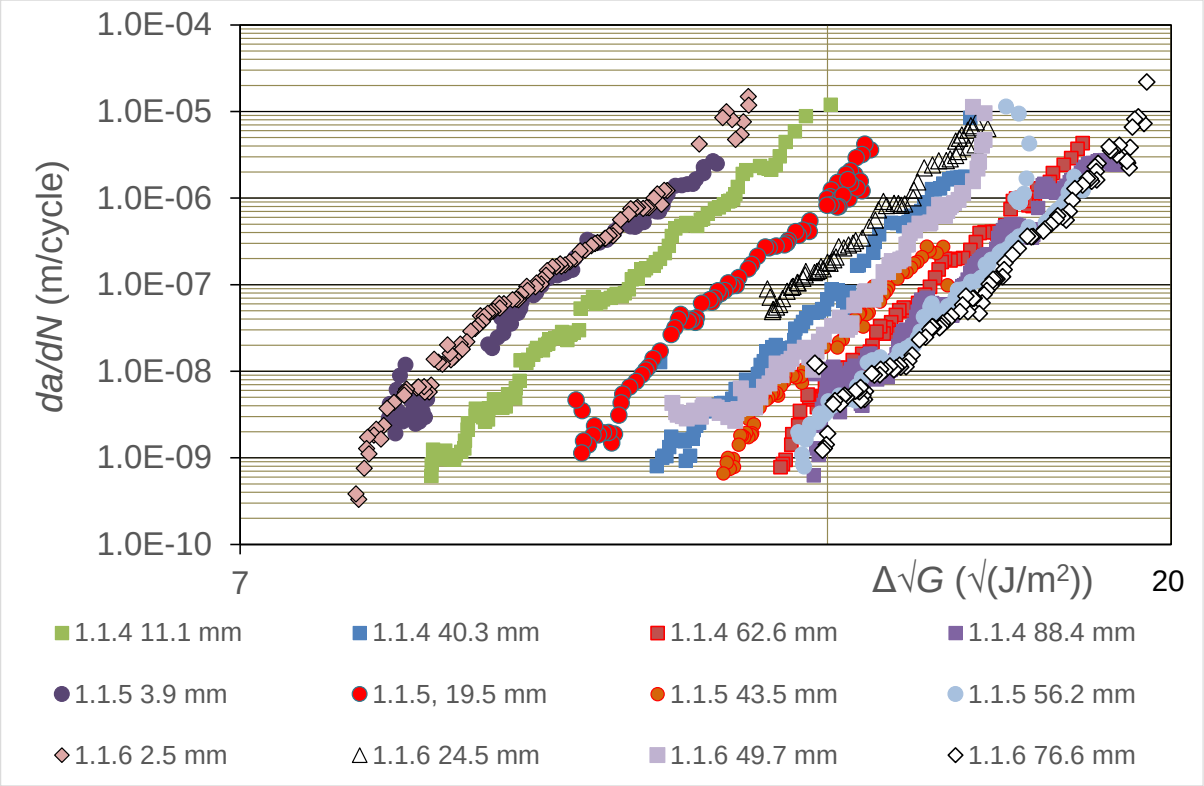


Figure 1. Measured FCG rate curves plotted as logarithmic *da*/*dN* versus logarithmic $\Delta\sqrt{G}$ from the DCB tests using an *R*-ratio of $R = 0.1$ for the CFRP composite for three DCB test specimens designated as tests '1.1.4', '1.1.5 and '1.1.6'. Values are given in the legend for the pre-crack extension length, a_p-a_o, prior to the start of measurements from the DCB fatigue test [14,15].

4. The Hartman-Schijve Methodology to Calculate the 'Worst-Case Upper-Bound' FCG Curves

Encouragingly, the findings reported in [11-15] suggest that the Hartman-Schijve modification of the NASGRO crack growth model [17] can provide a robust description of delamination propagation, independent of the specific testing protocol. For composite materials, the Hartman-Schijve equation is generally expressed as [11-15]:

$$\frac{da}{dN} = D\Delta\kappa^n \tag{1}$$

where:

$$\Delta\kappa = \left[\frac{\Delta\sqrt{G} - \Delta\sqrt{G_{thr}}}{\sqrt{\{1-\sqrt{G_{max}}/\sqrt{A}\}}}\right] \tag{2}$$

where D is the intercept in the Hartman-Schijve crack-growth equation using a double-logarithmic plot and n is the exponent in the Hartman-Schijve crack-growth equation again using a double-logarithmic plot. Further, A is the apparent cyclic fracture toughness and the term $\Delta\sqrt{G}$ is defined as:

$$\Delta\sqrt{G} = \sqrt{G_{max}} - \sqrt{G_{min}} \quad (3)$$

where G_{max} and G_{min} are the maximum and minimum applied energy release-rates in a fatigue cycle, respectively, and $\Delta\sqrt{G_{thr}}$ is the threshold value of $\Delta\sqrt{G}$ at which *da/dN* tends to zero. The term $\Delta\kappa$ is the crack driving force, i.e. the similitude parameter. Originally developed as an empirical model, similar in concept to the Paris Law [22-24], the Hartman-Schijve formulation has seen broad application across various material systems and is integrated into widely used engineering software such as NASGRO, particularly in the aerospace sector. A theoretical basis for its use with both additively- and conventionally-manufactured metallic materials has been established in [25], and it has been linked to formulations grounded in energy dissipation principles [26]. Furthermore, the model has demonstrated a strong capability in capturing both intrinsic and extrinsic variability, as categorized by Brunner [27,28], for a diverse array of materials. These encompass structural adhesives [29,30], thermoplastic polymers [31], polymer-matrix nanocomposites [32,33], fibre-reinforced polymer composites [11-15], metals produced through additive-manufacturing [34-42], and materials developed via cold spray additive-manufacturing (CSAM) [25]. An important feature that is discussed in [42-45] is that the Hartman-Schijve crack growth equation can be used to predict the growth of naturally-occurring 3D cracks in both conventionally-built and additively-manufactured metals.

As shown in detail below, the implementation of the Hartman-Schijve methodology to calculate the 'worst-case upper-bound' FCG curve first requires the measured FCG rate curves of *da*/*dN* versus $\Delta\sqrt{G}$, such as shown in Figure 1, to be re-plotted in the form of Equations (1) and (2). The aim being to obtain a linear, 'master' plot of logarithmic *da/dN* versus logarithmic $\Delta\kappa$ from all such measured FCG rate curves by choosing the values of $\Delta\sqrt{G_{thr}}$ and A that give the best fit to obtain this one linear 'master' plot. Secondly, the values of the terms D, n and $\Delta\sqrt{G_{thr}}$ that are obtained from this fitting exercise are key constants in calculating the 'worst-case upper-bound' FCG rate curves for design and service-life, i.e. sustainment, studies. For these latter studies, i.e. for predicting a FCG rate curve for small, naturally-occurring, delaminations, then it is generally assumed that the value of $\Delta\sqrt{G_{thr}}$ tends to zero. However, one can also calculate, for example, the 'worst-case upper-bound' FCG rate curve when we take the value of $\Delta\sqrt{G_{thr}}$ to be the mean value minus three standard deviations, σ, [14,15,46,47]. (In all cases, in calculating the FCG rate curves, the value of A is taken to be the mean value of the quasi-static value of the interlaminar fracture energy, G_{co}, minus typically three standard deviations, σ, [13-15,46,47].)

5. Previous ('Manual') Implementation of the Hartman-Schijve Methodology

In previous papers [e.g.11-15], the Hartman-Schijve methodology was essentially implemented by a 'manual' approach, combined more recently with a 'Total Least Squares' approach developed in [18]. However, this manual route requires a great deal of experience being needed by the human operator in order to achieve a relatively high value of the correlation coefficient, R^2, for the fit of the experimental data to the linear equation. Furthermore, for very large data sets there is great difficulty incurred in manipulating such a large amount of data using the 'manual method'.

The manual fitting process involves first setting an estimate for the $\Delta\sqrt{G_{thr}}$ threshold and $\sqrt{A}$ failure values for each FCG rate curve and assessing *D*, *n* and R^2 from the Hartman-Schijve linear, master plot fit that is obtained. The individual curve parameters for the threshold and failure values, i.e. $\Delta\sqrt{G_{thr}}$ and $\sqrt{A}$ respectively, are then modified and the values of the constants *D* and *n* are re-calculated, with the aim of improving the overall R^2 value of the fit.

Now, whilst the previous work has shown that such a manual method may give a good fit to a linear master plot of many sets of FCG rate curves obtained for various values of the pre-crack extension length, a_p-a_o and for different *R*-ratios and types of lay-up used for the CFRP, it is a difficult and tedious implementation route and may give large errors in the values of the key constants of *D*, *n* and $\Delta\sqrt{G_{thr}}$ if the operator is inexperienced. Further, if difficult and tedious, it is also likely to be less repeatable, even for experienced operators.

Therefore, the main aim of the present paper is to introduce a novel computer model to obtain a linear master plot of logarithmic *da/dN* versus logarithmic $\Delta\kappa$ from all the measured FCG rate curves by choosing the values of $\Delta\sqrt{G_{thr}}$ and *A* that give the best fit to the linear master plot, and hence to also obtain the values of the constants *D* and *n* in the Hartman-Schijve equation.

6. Automatic Implementation of the Hartman-Schijve Methodology

6.1 Introduction

Now, whilst the Hartman-Schjive crack-growth equation is defined above in terms of the energy-release rate, to enable the present study to make effective use of previous work [18,48] it is convenient to express this equation using the stress-intensity factor, *K*. The *K*-form for this equation, as typically used for metals, is given by:

$$\frac{da}{dN} = D\left[\frac{\Delta K - \Delta K_{thr}}{\sqrt{\{1-K_{max}/A\}}}\right]^n \qquad (4)$$

And $\Delta\kappa$ is the crack driving force, i.e. the similitude parameter, now expressed in the *K*-form by:

$$\Delta\kappa = \left[\frac{\Delta K - \Delta K_{thr}}{\sqrt{\{1-K_{max}/A\}}}\right] \quad (5)$$

and where the term ΔK is defined as:

$$\Delta K = K_{max} - K_{min} \quad (6)$$

where K_{max} and K_{min} are the maximum and minimum applied stress-intensity factors in a fatigue cycle, respectively, and ΔK_{thr} is the threshold value of ΔK at which *da/dN* tends to zero. The constant *D* is the intercept in the Hartman-Schijve crack-growth equation using a double-logarithmic plot and *n* is the exponent in the Hartman-Schijve crack-growth equation again using a double-logarithmic plot, and A is the apparent cyclic fracture toughness, but now all in terms of the using the *K*-form approach. Thus, the term $\Delta\kappa$ is the crack driving force, i.e. the similitude parameter, but now for the *K*-form approach.

A methodology for fitting multiple curve data sets to the *K*-form of the Hartman-Schijve growth law was presented in [18]. As part of the work reported in [18], the methodology was implemented in a computer software, CGROW [48], where CGROW is an existing software providing a framework for the determination of fatigue crack growth model parameters. This software allows the fitting process to be carried out and reports master *D* and *n* values and the R^2 for the best fit. These papers showed the benefits of using a total least squares calculation to fit individual curves rather than an ordinary least squares calculation. The former has benefits due to the asymptotic nature of the Hartman-Schijve curve in both the threshold and failure regions. However, due to differences in the orders of magnitude on the x-axis (i.e. the ΔK axis) compared to the y-axis (i.e. the *da/dN* axis), then when carrying out total least squares calculations a normalisation scale factor, s, had to be introduced. Several solution algorithms for the fitting procedure were tested and their relative merits discussed.

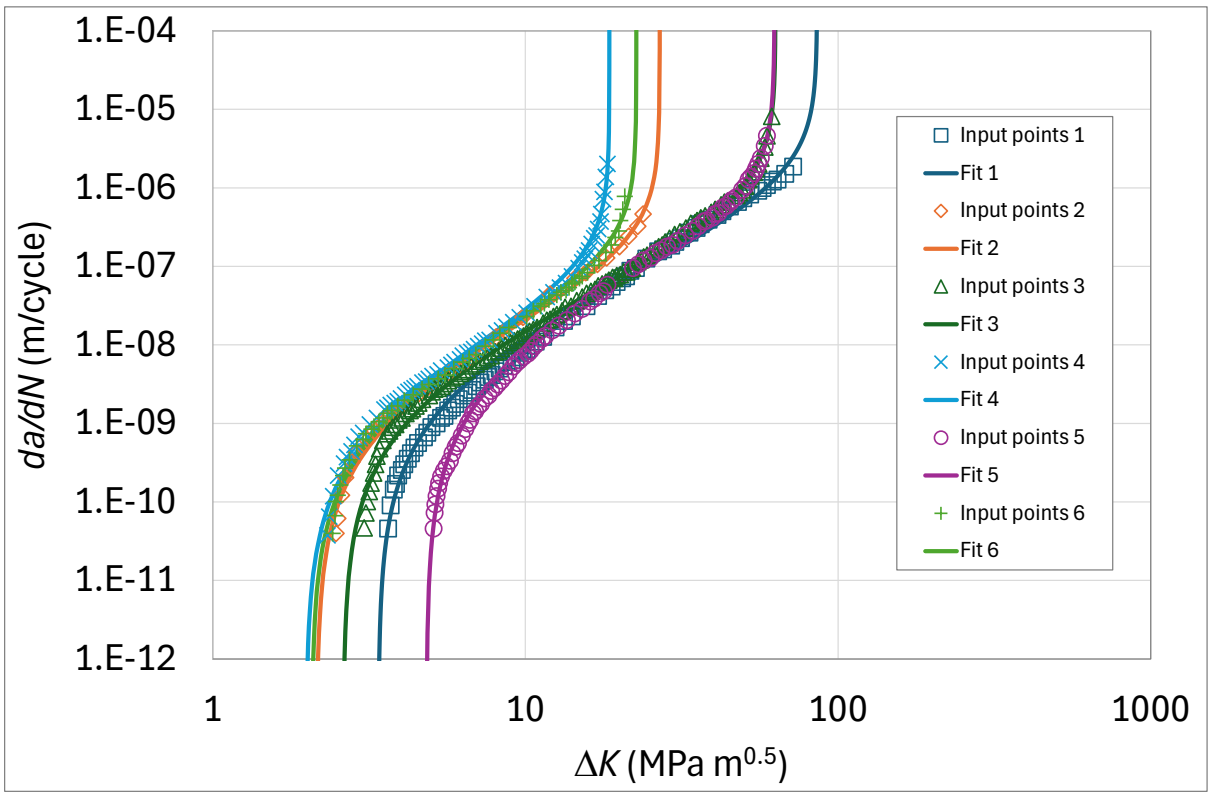
Thus, the current study is based on the total least squares approach of [18] but uses a different and more efficient solution method to drive the iterative search for the fit parameters. In addition, the effect of the normalisation scale factor described in [18] has been investigated with the result that an additional scale factor is proposed. The current method is implemented for both the $\sqrt{G}$-form of the Hartman-Schijve equation shown in Equations 1 and 2 and the *K*-form shown in Equations 4 and 5. The solution procedures are the same due to the analogy of the terms in Equations 1 and 4. Allowing a fitting capability for both equations simply requires

suitable options to handle different forms of input data and the correct description of threshold and failure output quantities in a $\sqrt{G}$ or K framework.

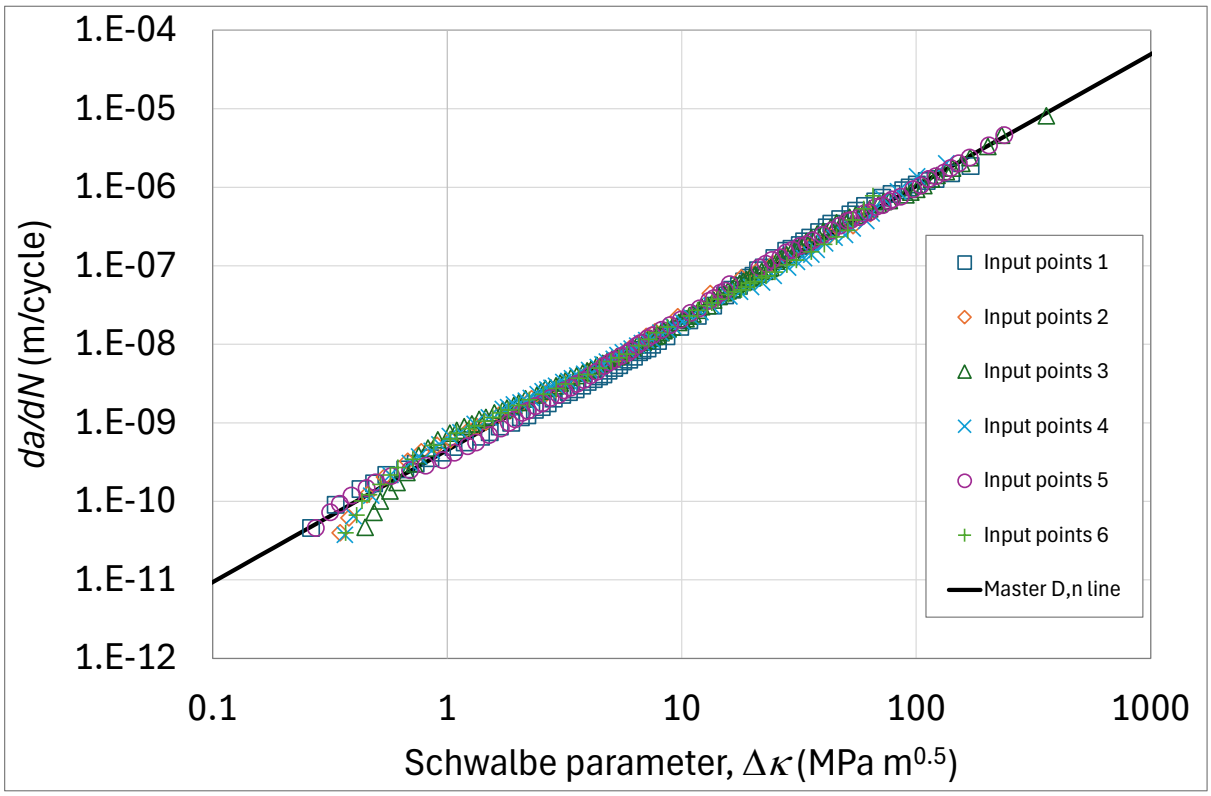
6.2 Solution procedure

6.2.1 Overview

Figure 2 gives an example, based on the *K*-form of the Hartman-Schijve equation, in which six sets of curve points are fitted, see Figure 2(a). The philosophy behind the fitting process when there are multiple sets of test data is to generate individual curve fits while aiming to achieve a linear fit in the logarithmic *da/dN* versus logarithmic $\Delta\kappa$ space, see Figure 2(b), in order to produce *D* and *n* for a 'master' Hartman-Schijve linear plot. To achieve the linear fit shown in Figure 2(b), an iterative fitting process is carried out, as summarised in the schematic of Figure 3. This process requires calculation of different threshold and failure parameters associated with the individual curve fits. The threshold and failure parameters of each curve are obtained by optimising the total least squares fit at a given *D* and *n*. The ordinary least squares fit for all data points with respect to the logarithmic *da/dN* versus logarithmic $\Delta\kappa$ space is an outcome of this process and is not explicitly optimised, but instead tends to improve as the individual curve fits, and the *D* and *n* values, converge. At the end of the process, the mean threshold and failure parameters of the separate curves are applied as the threshold and failure values of the mean master curve. Standard deviation values of the threshold and failure parameters can be calculated and up to two or three standard deviation offsets applied to assist with the definition of a worst-case upper-bound FCG rate curve. The elapsed run time for the fit of six sets of curve points shown in Figure 2 is 69 seconds (on an 11th Gen Intel Core i9-11950H 2.60GHz processor).



(a)



(b)

Figure 2. Example (a) of fitting six measured data curves to the Hartman-Schijve equation while (b) attempts to achieve a linear logarithmic *da/dN* versus logarithmic $\Delta\kappa$ fit. This example uses the *K*-form of the Hartman-Schijve equation, see Equations (4) and (5).

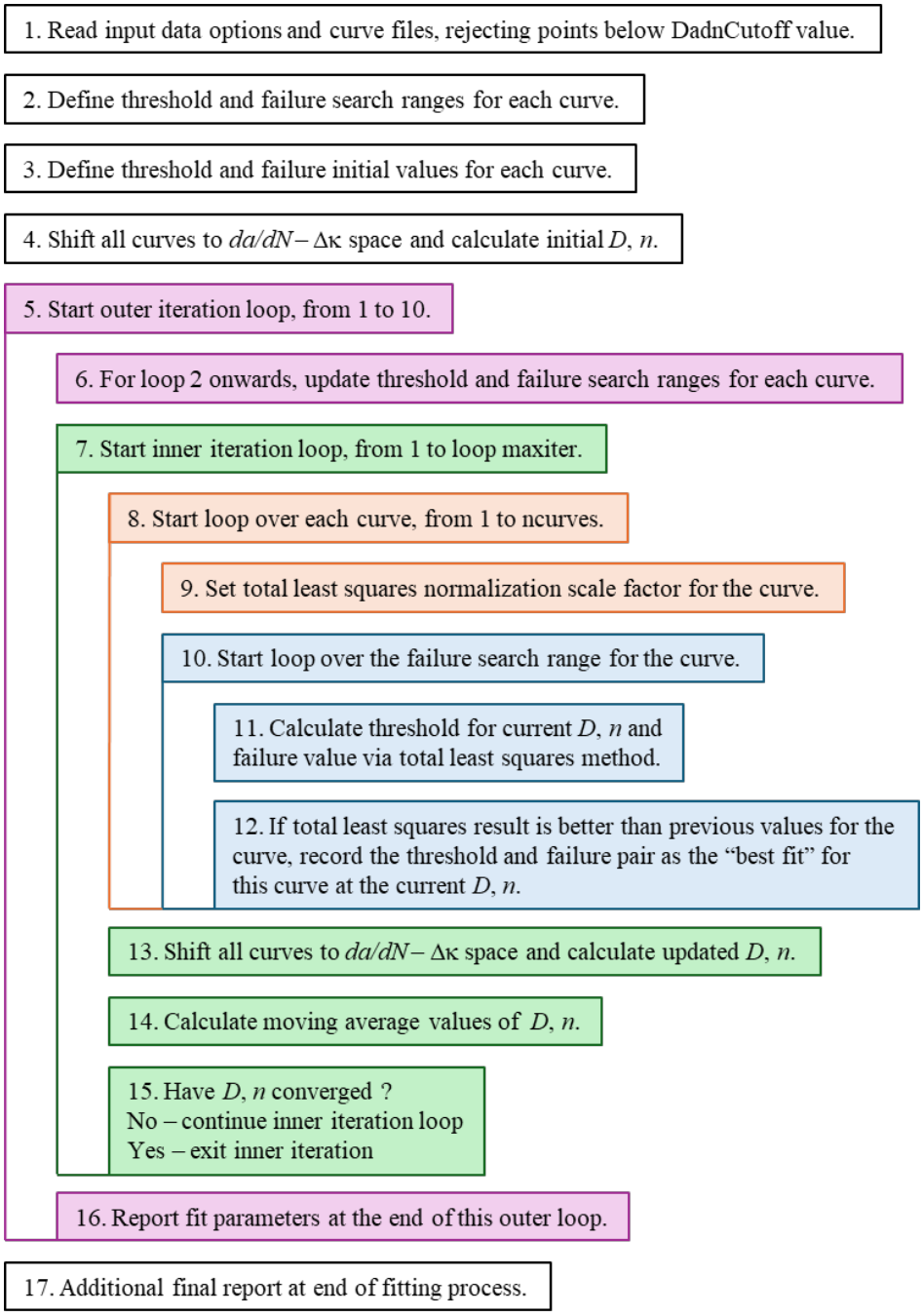


Figure 3. Schematic diagram of the fitting process, showing the four nested loops, identified by the pink, green, orange and blue boxes.

As noted above, the curve-fitting process aims to find the threshold and failure parameters for each curve and the overall values of the constants D and n. To initialise the process, it is necessary to define ranges for the possible threshold and failure values for each separate curve, and initial values of threshold and failure parameters for each curve, i.e. steps 2 and 3 in Figure 3. The fit for each curve will then be found within the specified range brackets for that curve. Figure 4 shows a single curve with possible ranges of the threshold and failure values added as vertical dashed lines onto the plot. (The position of the lower threshold and

upper failure bounds in Figure 4 are illustrative and do not represent the actual default positions that would be used to fit this data set.) The ranges are defined by:

- Threshold lower and upper bounds
- Failure lower and upper bounds

The default procedure adopted during the solution is that the threshold and failure range values for a FCG curve are calculated automatically from the first and last points of that curve. The lower threshold and upper failure bounds are set such that they should be well below and above, respectively, any values calculated during the fitting process, i.e. the calculated FCG curve is not restricted by the chosen bounds. This is shown in Figure 4, in which the asymptotes of the orange fit-line lie within the threshold and failure search ranges. This approach means that a fully unconstrained fit can be sought. Extra constraint may be placed on the solution by defining specific threshold or failure values for one or more curves.

In the single curve example in Figure 5, a specific failure upper bound has been defined and the fit becomes constrained by that value. Alternatively, specific threshold *and* failure values for one or more curves can be defined to generate a more constrained fit. It is also possible to constrain the solution by specifying specific *D* and/or *n* values. In general, the more additional constraint that is applied, the less parameters the algorithm has to vary, with the result that the R^2 is likely to be reduced compared to a numerically unconstrained solution.

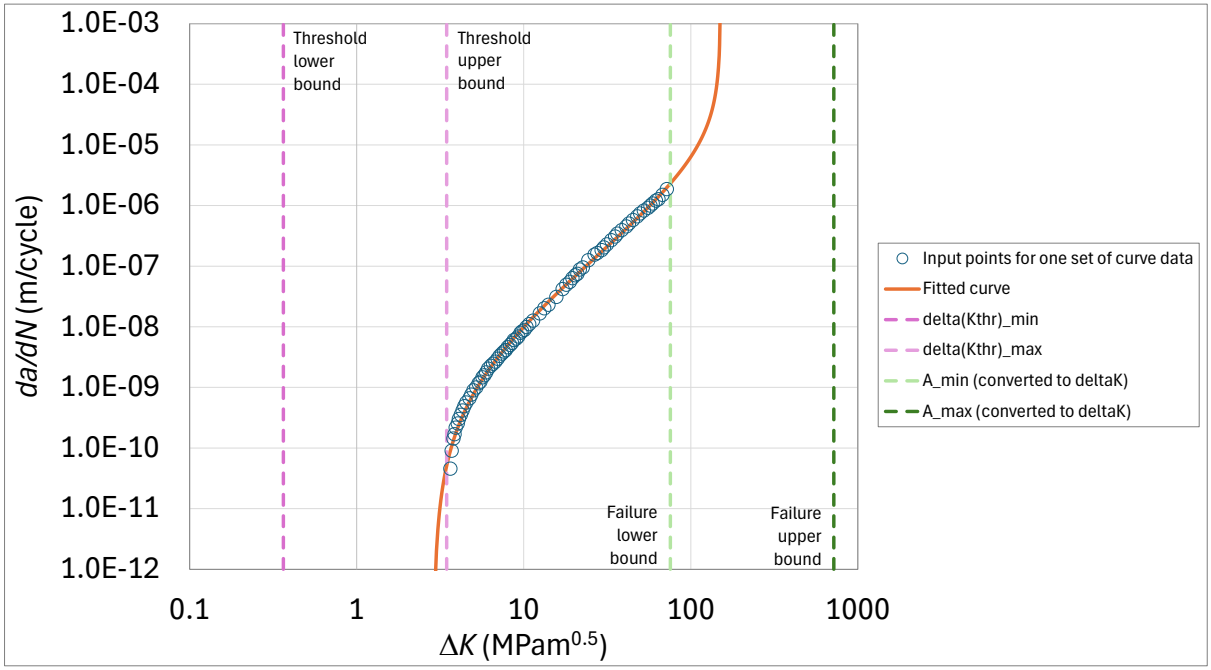


Figure 4. Example of fitting a single curve set of points with specified threshold and failure bound ranges.

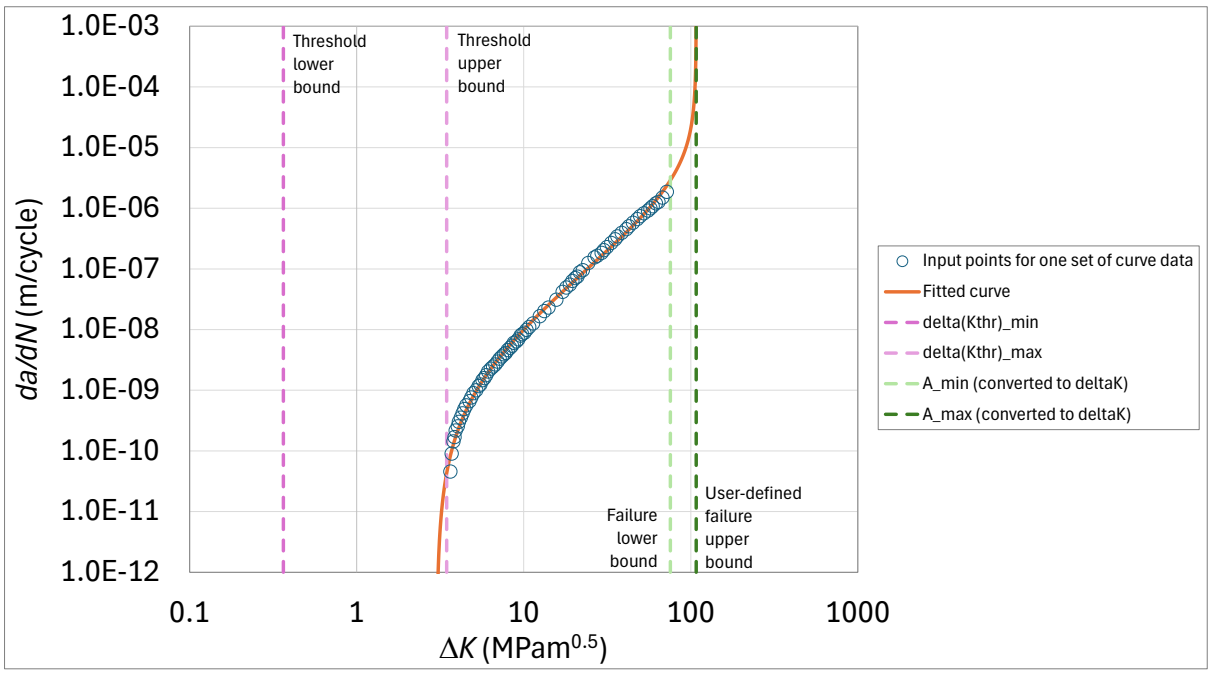


Figure 5. Example of fitting a single curve set of points with failure value constrained by a specified failure upper bound value.

Having set threshold and search ranges for each curve, and an initial estimate of the threshold and failure values for each curve, an initial estimate of D and n is calculated, i.e. step 4 in Figure 3. The iterative process then begins. This consists of a series of four nested loops. The outer loop is configured to run for ten iterations, i.e. steps 5 to 16 in Figure 3, with each iteration aiming to reduce the curve search ranges and reduce the convergence tolerance on D and n. The intent is to start with a wide search and to home-in on an improving solution. Within the outer loop is the inner iteration loop that solves for new D and n values and checks for convergence of D and n, i.e. steps 7 to 15 in Figure 3. As part of this process, the third of the four nested loops cycles over each curve to calculate threshold and failure parameters for the curve at the current D and n, i.e. steps 8 to 12 in Figure 3. As part of this process, the fourth and final nested loop cycles over the failure range of the curve and identifies the threshold and failure pair that give the optimum total least squares fit for the curve at the current D and n, i.e. steps 10 to 12 in Figure 3. Convergence of the inner iteration loop is deemed to occur when the D and n changes are sufficiently small, see Section 6.1.3. The final reported R^2 value is the ordinary least squares fit of the input data points in log-log space of Equation 1, or Equation 4, with respect to the final D and n values. The solution procedure is numerically efficient and runs relatively quickly. The total elapsed time will, however, be a function of the number of curves, the total number of curve data points and the spread of those points. Some additional comments on this aspect are made in later sections.

6.2.2 Total least squares fit for a curve

The total least squares process implemented in the current method follows the bi-section method described in Algorithm 1 of [18] with the sum of the total least squares calculated using Algorithm 2 of [18]. The aim of the two algorithms is to find, for a single curve at given values of *D* and *n*, a threshold and failure pair that minimises the sum of the total least squares distance within the current threshold and failure search ranges. Where the current method differs from [18] is in the additional looping processes described in Figure 3 which aim to start with wide search ranges and tolerances, with ranges and tolerances reducing as the fit progresses. This enables fewer total iterations to be required than if a single pass solution is attempted.

An issue identified in [18] is that the total least squares calculation is operating on x and y ranges that are considerably different in their order of magnitude. A scaling parameter, s, see equation 8 in [18], was therefore introduced in [18] to normalise the axis ranges. The magnitude of the sum of the total least squares is not important in this process, the aim is to find the threshold and failure pair that provide the lowest sum of the total least squares. Therefore, it is reasonable to allow the scaling factor to be modified. The possibility then arises that changing the scaling factor will change the numerical behaviour. In the current work, an additional scale factor has been tested such that the total scale factor is the product of the additional scale factor and the scale factor, s, as defined in equation 8 in [18]. Consistent behaviour has been observed across multiple sets of test data such that a “default” additional scale factor of 0.1 has been defined for the current method. An example of the effect of the additional scale factor on the fitting process is given in Section 5.3.

6.2.3 Iteration convergence for *D* and *n*

The second iteration loop continues until the values of *D* and *n* have small changes in successive iterations:

```
diff_D = abs( D - D_previous ) / D_previous
diff_n = abs( n - n_previous ) / n_previous
if (diff_D.lt.tolConverge .and. diff_n.lt.tolConverge) -> convergence achieved
```

The value of tolConverge is set to 1e-2 for the first outer loop and 1e-4 for the tenth outer loop with a linear progression in between. This was found to provide a more efficient solution than allowing a tight tolerance of 1e-4 at all outer loops. The value of 1e-4 can be considered an arbitrary value, chosen by testing across a number of data sets. Similarly, other control values in the algorithm are also chosen based on performance and accuracy across a number of data sets. In addition, to prevent the possibility of the numerical process deeming to have converged

if consecutive iterations have small variations when there is still a general changing trend, a moving average calculation is performed on *D* and *n* such that the above convergence check is using values averaged over the previous ten iterations. Further controls are applied to prevent the moving average starting until some initial iterations are completed, with the average being gradually introduced over a number of iterations. Convergence is also not checked in the initial iterations.

6.3 Single curve calculation: comparison with other algorithms

The simplest fitting process to attempt is that for a set of points representing a single curve. In [18] this approach was adopted using the *K*-form of the Hartman-Schijve equation, see Equation 4, to compare several different numerical fitting procedures using a manually constructed set of points. Four curve parameters were defined (i.e. *D* = 3.9e-10, *n* = 2.29, ΔK_{thr}= 3.04 MPa$\sqrt{m}$, *A* = 116.81 MPa$\sqrt{m}$) and, using these parameters, thirty points were calculated to give a Hartman-Schijve linear plot for a load ratio, *R*, of 0.8. These were defined as "unperturbed data points". The x values (i.e. ΔK) were then randomly adjusted to provide a "perturbed curve". The perturbed curve points were used as the input for testing different fitting algorithms to calculate values for the four fitted curve parameters. The perturbed points have been extracted as accurately as possible from [18] to allow a comparative fit calculation using the current method. Table 1 gives the fit results for three methods as reported in [18]: CUHYSO, MLSL LDS and AGS. These acronyms refer to the different numerical approaches to the fitting process, as described in [18]. CUHYSO was introduced as a new method in [18] and refers to Contracting Uniform Hyper-Rectangles Sampling for Optimization. MLSL LDS stands for Multi-level Single-Linkage with Sobol Low Discrepancy and uses a multi-start method with random sampling. AGS uses minimization of multi-extremal functions under nonconvex constraints, using a Hilbert curve. A calculation using default options in the CGROW software [48] is presented using the same perturbed input data as the calculation using the current method. The CGROW software was generated during the work reported in [18]. The perturbed fit calculation should not recover the unperturbed parameters as the data has been modified, but results should be close to the unperturbed parameters. Figure 6 shows graphs of the logarithmic *da/dN* versus logarithmic $\Delta\kappa$ plot of the fit line and input data points shifted to $\Delta\kappa$ using the fit parameters.

Results in [18] did not include R^2 values for fits to the logarithmic *da/dN* versus logarithmic $\Delta\kappa$ plot. For the CUHYSO, MLSL LDS and AGS entries in Table 1, the R^2 values have been calculated using the input points used for the new fit calculation and the stated fit parameters from [18]. For the CUHYSO, MLSL LDS and CGROW calculations of R^2 the final

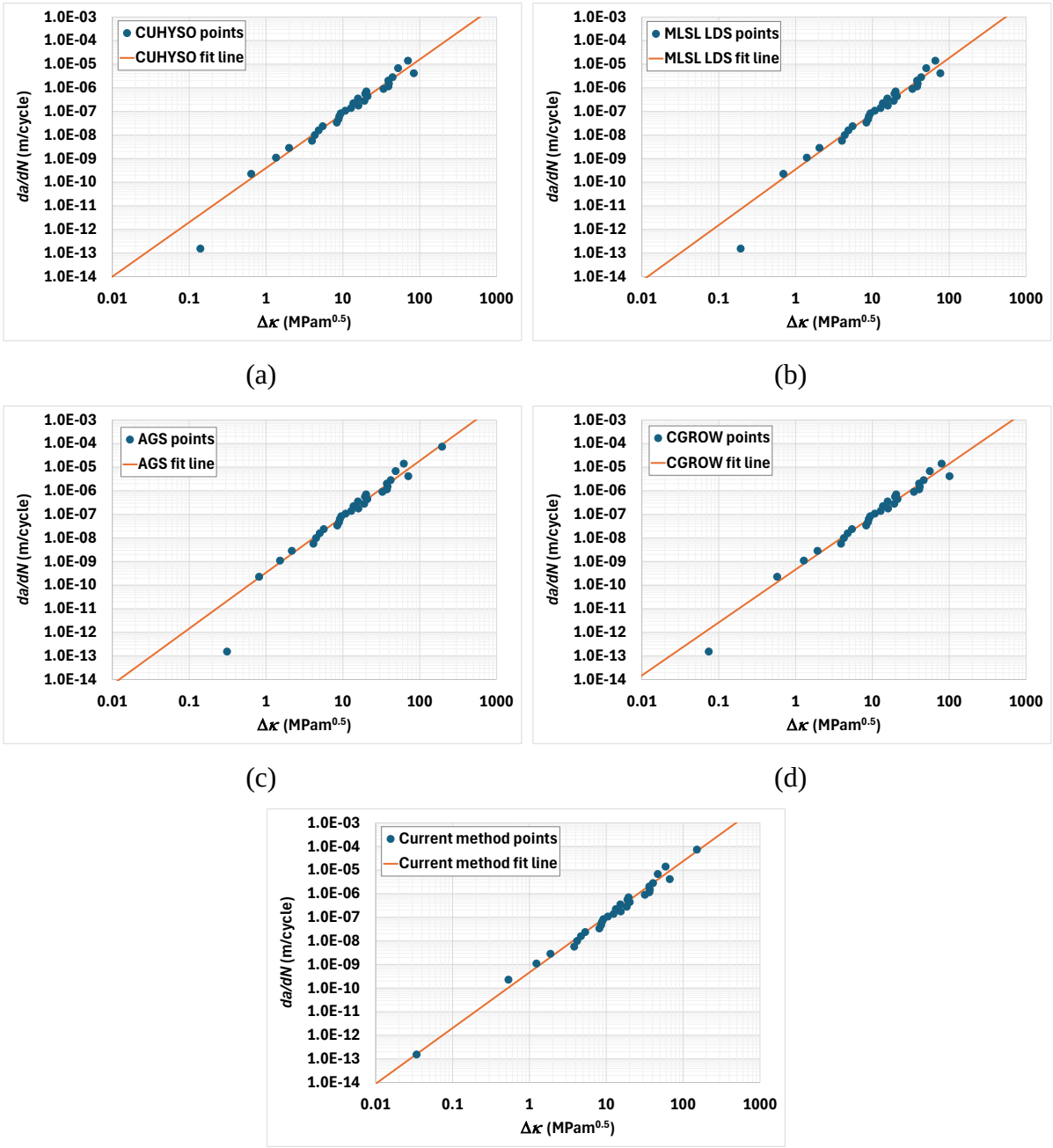
input point lies beyond the failure portion of the fitted curve. The value of $\Delta\kappa$ cannot be defined for such points and therefore they do not contribute to the R^2 calculation, nor can those points be plotted in the relevant charts in Figure 6.

There is a small variation in the fit parameters *D*, *n*, ΔK_{thr} and *A* shown in Table 1, indicating that the different numerical procedures produce slightly different fits. The charts in Figure 6, in which a perfect fit places all points on the fit line, show that there are very small differences in the behaviour of the majority of the points, i.e. the positioning of the points in relation to one another and the fit lie for each is similar across the charts. The details of the fit behaviour close to the threshold and failure portions of the curve (i.e. the first and last data points) appear to be the differentiators in terms of the overall R^2 values, with only the current method providing a close fit for both extreme points, thus accounting for the highest value of R^2 of 0.988.

In the current method, as described in Section 5.1, the iterative fitting process takes place in ten outer loops each of which continues until *D* and *n* have pre-defined small changes. The behaviour of the fit parameters *D*, *n*, ΔK_{thr}, *A* and the R^2 value through all iterations is shown for the perturbed single curve fitting process in Figure 7, confirming that all the parameters tend towards converged values

Table 1. Hartman-Schijve parameters for the fitting of a single linear plot of the perturbed data points.

Calculation method	*D*	*n*	ΔK_{thr} (MPa$\sqrt{\text{m}}$)	*A* (MPa$\sqrt{\text{m}}$)	R^2
CUHYSO [18]	4.0e-10	2.30	3.04	120.11	0.960
MLSL LDS [18]	3.5e-10	2.36	2.99	121.53	0.950
AGS [18]	3.4e-10	2.37	2.99	123.12	0.933
CGROW	4.6e-10	2.24	3.10	117.98	0.975
Current method	4.6e-10	2.36	3.14	124.08	0.988



(a) (b)

(c) (d)

(e)

Figure 6. Charts of logarithmic *da/dN* versus logarithmic $\Delta\kappa$ for the perturbed data points and linear fit plots of Table 1 using: (a) CUHYSO, (b) MLSL LDS, (c) AGS, (d) CGROW, (e) current method. (See text for details.)

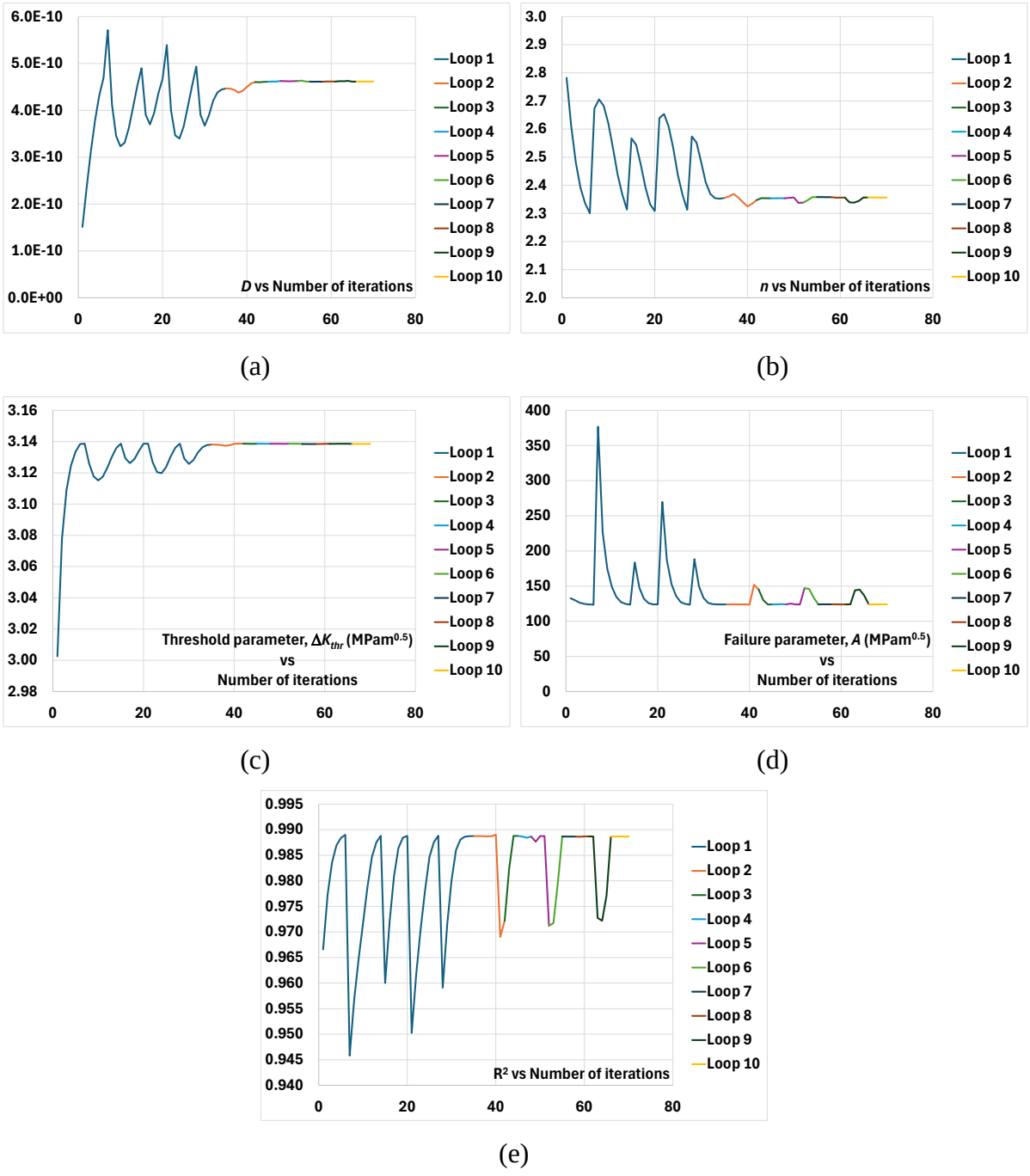


Figure 7. Plots of the through-iteration behaviour of the four fit parameters and the value of R^2 of the fit to logarithmic *da/dN* versus logarithmic $\Delta\kappa$ for the perturbed data points using the current method.

6.4 Multiple curve calculations: comparison with previous manual calculation for a data set of twenty-five FCG rate curves at R=0.1

6.4.1 Introduction

Experimental data obtained at the Swiss Federal Laboratories for Materials Science and Technology (Empa, Dübendorf) and at University College Dublin (UCD, Ireland) as part of a European Structural Integrity Society (ESIS), Technical Committee (TC) 4 (on Polymer, Composites and Adhesives) round-robin study into the reproducibility of delamination growth under cyclic-fatigue loads was presented in [14], with further discussion and processing of the data in [15]. Section 4 of [14] collated twenty-five test curves at R=0.1 (twelve from Empa and thirteen from UCD). A manual fitting process was used to determine the parameters to give the master Hartman-Schijve linear plot for these twenty-five curves, see above. The resulting fit parameters are reproduced in the first row of Table 2.

In the present paper, the test data used in [14] has been processed using the current, automatic method described in Section 5.1. While care has been taken to use the same curve data as used for the fit created in [14], it is noted that a small number of data points have been included which were omitted in the manual processing of [14]. The current processing for the twenty-five curves included a total of 1927 points with the number of points per FCG rate curve ranging from 33 to 166 points. Three sets of fit results using variants of the current method are included in Table 2, where the values of R^2 for the fit of the data points to the linear, master Hartman-Schijve plot are also given.

Table 2. The values of the Hartman-Schijve parameters and R^2 resulting from the various calculation methods from fitting of the twenty-five Empa and UCD tests at R=0.1 for the CFRP.

Method	D	n	$\Delta\sqrt{G_{thr}}$ and std. dev. ($\sqrt{\mathrm{J/m^2}}$)	$\sqrt{A}$ and std. dev. ($\sqrt{\mathrm{J/m^2}}$)	R^2	Elapsed run times (s)
Manual (Fig 5 of [14] and Table A1 of [15])	1.23e-10	4.49	10.53±2.15	30.11±8.25	0.975	N/A
Current method with all data	2.31e-15	8.11	7.14±2.03	38.73±11.50	0.965	19265
Current method with *da/dN* cut-off of 1e-8 m/cycle	3.16e-13	5.68	8.21±2.26	24.40±4.75	0.956	6610
Current method with all data and constrained *A*	2.99e-11	3.97	9.33±2.39	24.22±6.43	0.896	5643

In Table 2, for the current automatic calculations the terminology used is:

- 'Current method with all data' uses the default fitting process with no imposed values of threshold or failure parameters for individual FCG rate curves. All individual curve parameters and the overall master fit parameters are calculated from the full set of 1927 data points.
- 'Current method with *da/dN* cut-off of 1e-8 m/cycle' adds a condition that all input points with *da/dN* below 1e-8 m/cycle should be excluded from the fit. The *da/dN* cut-off condition is included as an option to allow assessment of the effect of low *da/dN* values on the fit parameters. In terms of the solution process, the original input data remains unchanged - this extra condition merely eliminates points from the data set prior to the start of the fitting process. For a *da/dN* cut-off of 1e-8 m/cycle, the data set is reduced to a total of 1610 points.
- 'Current method with all data and constrained *A*' is a two-stage process in which $\sqrt{A}$ values are imposed on each individual curve as additional input data for the fitting process. These input values are forced upon the solution process and are returned as the final individual curve $\sqrt{A}$ values. This places some constraint on the solution process by removing the possibility for the individual curve $\sqrt{A}$ values to be modified. This partly mimics the manual

method in which both threshold and failure values are specified for each curve. Rather than applying 'engineering knowledge' as is done with the manual method, the 25 individual curve $\sqrt{A}$ values for this calculation are determined by running single-curve fits for each of the twenty-five input curves. The resulting $\sqrt{A}$ values range from to 14.8 to 38.9 $\sqrt{\mathrm{J/m^2}}$. It is noted that the current method can also allow the specification of threshold and failure parameters for each curve. In this way, the fitting process can be used to replicate the manual method by a trial and error approach in which all individual curve parameters are specified to calculate *D* and *n* values.

The fit parameters from these three sets of conditions using the automatic calculation methods are shown in rows 2, 3 and 4 respectively of Table 2. For example, the master, linear line, plotted as logarithmic *da/dN* versus logarithmic $\Delta\kappa$ for the 'Current method with all data' results, is shown in Figure 8. This can be compared with Figure 5 of [14] and the relevant values in Table 1 of [14] for the manual method, and see also row one of Table 2 in the present paper. (The results for the 'Current method with all data and constrained *A*' are not considered further due to the relatively low value of R^2 that was obtained.)

The elapsed run times shown in the final column of Table 2 are obtained using a laptop computer with an 11th Gen Intel Core i9-11950H 2.60GHz processor. Introducing a cut-off for *da/dN* reduces the data set being processed and therefore speeds up the calculations. The imposition of additional constraint on the A values further speeds up the fitting process.

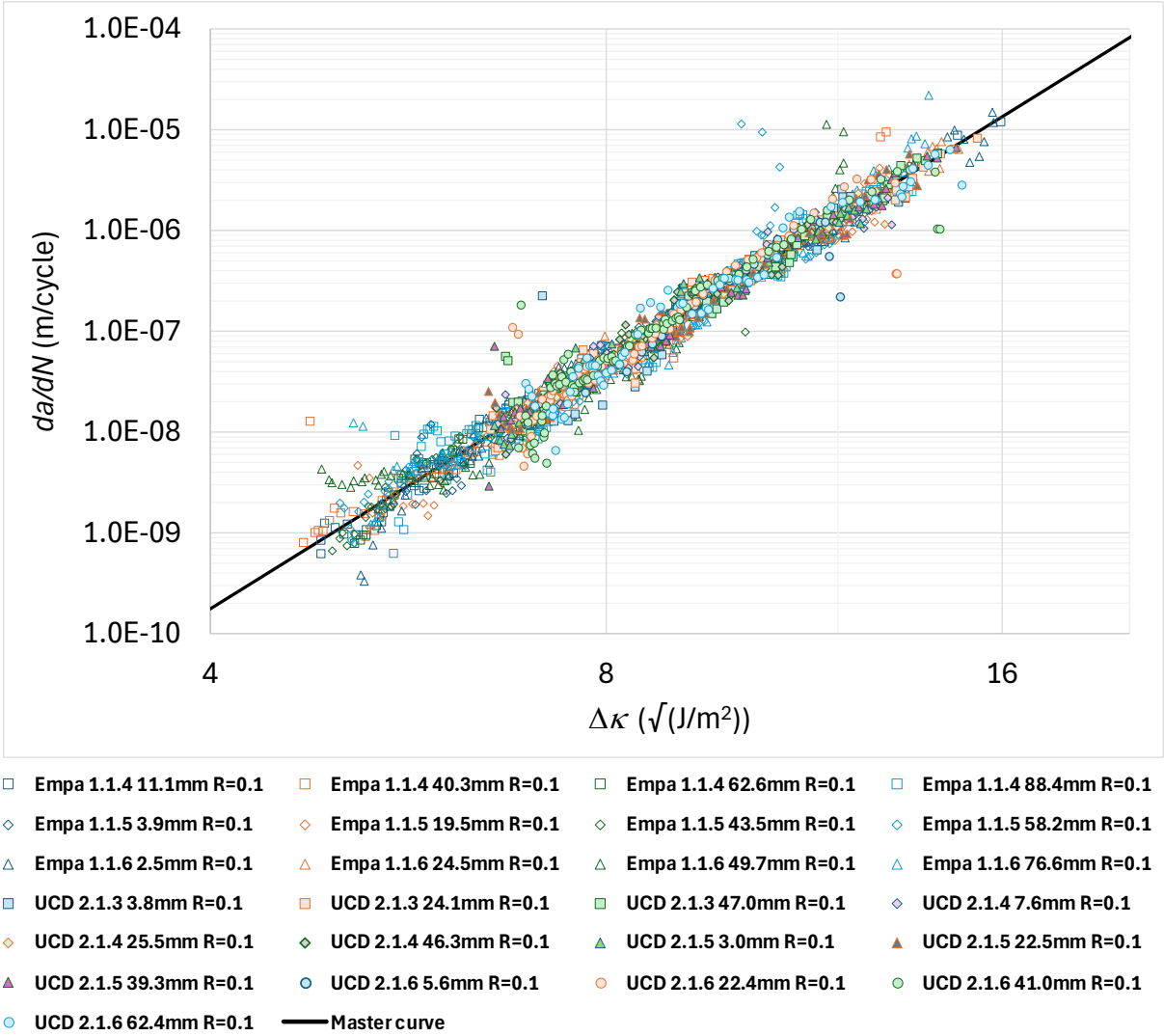


Figure 8. Logarithmic *da/dN* versus logarithmic $\Delta\kappa$ for the twenty-five sets of data [14,15] at R = 0.1. Fit data shown is using the 'Current method with all data' results to obtain the master, linear Hartman-Schjive plot and the Hartman-Schijve constants are found to be: D = 2.31e-15, n = 8.11, and $\Delta\sqrt{G_{thr}}$ =7.14±2.03 $\sqrt{\text{J/m}^2}$; with R^2 = 0.965.

The various FCG rate curves calculated from the three methods of interest, using the values of the Hartman-Schjive constants, i.e. D, n and $\Delta\sqrt{G_{thr}}$, given in Table 2, are shown in Figure 9 along with the experimental results. (The mean G_{co} value used is that reported in [15]: 250 J/m^2 with a standard deviation ±45 J/m^2.)

6.4.2 The 'Mean' FCG rate curves

The mean FCG rate curves that may be calculated are plotted in Figure 9 and are:

- The 'Mean FCG rate curve [14,15]' (orange-dotted line) as deduced from the fit parameters reported in Figure 5 of [14] and Table A1 of [15] from the 'Manual method' with the mean $\Delta\sqrt{G_{thr}}$ value from the individual 25 curve fits and with the mean

$\sqrt{G_{co}}$ $\left(\cong\sqrt{A}\right)$ value; and hence with *D* = 1.23e-10 and *n* = 4.49 (see first-row of Table 2 for full details).

- The 'Mean FCG rate curve' (orange-solid line) is deduced from the automatic 'Current method with all the data' with the mean $\Delta\sqrt{G_{thr}}$ value from the individual 25 curve fits and with the mean $\sqrt{G_{co}}$ $\left(\cong\sqrt{A}\right)$ value; and with *D* = 2.31e-15 and *n* = 8.11 (see second row of Table 2 for full details).
- The 'Mean FCG rate curve (cut-off)' (orange-dashed line) is deduced from the automatic 'Current method with *da/dN* cut-off of 1e-8 m/cycle' using the mean $\Delta\sqrt{G_{thr}}$ value from the individual 25 curve fits and with the mean $\sqrt{G_{co}}$ $\left(\cong\sqrt{A}\right)$ value; and with *D* = 3.16e-13 and *n* = 5.68 (see third row of Table 2 for full details).

It may be observed from Table 2 that the 'Manual method' of [14,15] has provided a slightly higher R^2 value compared to the calculations with the automatic 'Current method with all data' option. From Figure 9, compared to the FCG rate curve from the Manual method, i.e. the 'Mean FCG curve [14,15]', the 'Current method with all data' option produces a 'Mean FCG rate curve' which only deviates somewhat in the lower portion for *da/dN* values below about 1e-9 m/cycle. Further, the FCG rate curves calculated from the two automatic methods are almost identical. Although, at the upper end of the curves, slight deviations occur between the two curves when the value of *da/dN* reaches about 1e-4 m/cycle. Thus, whilst the differences in the values of *D* and *n* in Table 2 from the different methods may appear to be relatively large, they manifest as only relatively small differences in the calculated mean FCG rate curves. Now, although arguments can be made for ignoring data beneath a crack growth rate of 10^{-8} m/cycle, it is generally not the best approach to ignore data. As such the constants determined by the 'automatic' calculations using the 'Current method with all data' should be considered to be a better representation, noting also a slightly higher R^2 value compared to the 'cut-off' automatic method.

6.4.3 The 'Worst-case [mean-3σ]' FCG rate curves

The worst-case upper-bound [mean-3σ] FCG rate curves, i.e. using the mean threshold and mean $\sqrt{A}$ with minus three standard deviations applied (and labelled 'Worst-case [mean-3σ]') are shown in Figure 9 and are:

- The 'Worst-case [mean-3σ] [14,15]' FCG rate curve (purple-dotted line) is deduced from the fit parameters reported in Figure 5 of [14] and Table A1 of [15] from the 'Manual method' using the mean $\Delta\sqrt{G_{thr}}$ with a -3σ applied from the individual 25 curve fits and

the mean $\sqrt{G_{co}}$ $\left(\cong\sqrt{A}\right)$ value with a -3σ applied; and hence with *D* = 1.23e-10 and *n* = 4.49 (see first row of Table 2 for full details).

- The 'Worst-case [mean-3σ]' FCG rate curve (purple-solid line) is deduced from the automatic 'Current method with all data' using the mean $\Delta\sqrt{G_{thr}}$ with a -3σ applied from the individual 25 curve fits and with the mean $\sqrt{G_{co}}$ $\left(\cong\sqrt{A}\right)$ value with a -3σ applied; and with *D* = 2.31e-15 and *n* = 8.11 (see second row Table 2 for full details).
- The 'Worst-case [mean-3σ] (cut-off)' (purple-dashed line) FCG rate curve is deduced from the automatic 'Current method with *da/dN* cut-off of 1e-8 m/cycle' using the mean $\Delta\sqrt{G_{thr}}$ with a -3σ applied from the individual 25 curve fits and the mean $\sqrt{G_{co}}$ $\left(\cong\sqrt{A}\right)$ value with a -3σ applied; and with *D* = 3.16e-13 and *n* = 5.68 (see third row of Table 2 for full details).

It may be observed from Figure 9 that the two automatic options, i.e. the 'Worst-case [mean-3σ]' and the 'Worst-case [mean-3σ] (cut-off)' curves, are further to the left than the 'Manual method' curve, i.e. the 'Worst-case [mean-3σ] [14,15]' curve, due mainly to the lower threshold values calculated using the two automatic methods. Thus, for these 'Worst-case [mean-3σ]' curves, the two automatic methods provide less conservative FCG rate curves in the low $\Delta\sqrt{G}$ region than the 'Manual method', i.e. a higher value of *da/dN* for a given value of $\Delta\sqrt{G}$.

6.4.4 The 'Worst-case (durability)' FCG rate curves

The worst-case (durability) FCG rate curves, i.e. using $\Delta\sqrt{G_{thr}}$ equal to zero and a mean $\sqrt{G_{co}}$ $\left(\cong\sqrt{A}\right)$ value with minus three standard deviations applied (and labelled 'Worst-case [durability]') are shown in Figure 9:

- The 'Worst-case [durability] [14,15]' FCG rate curve (grey-dotted line) is calculated from the fit parameters reported in Figure 5 of [14] and Table A1 of [15] from the 'Manual method' and is deduced using $\Delta\sqrt{G_{thr}}$ equal to zero and with the mean $\sqrt{G_{co}}$ $\left(\cong\sqrt{A}\right)$ value with a -3σ applied; and with *D* = 1.23e-10 and *n* = 4.49 (see first row of Table 2).
- The 'Worst-case [durability]' (grey-solid line) FCG rate curve is deduced from the automatic 'Current method with all data' using $\Delta\sqrt{G_{thr}}$ equal to zero and with the mean $\sqrt{G_{co}}$ $\left(\cong\sqrt{A}\right)$ value with a -3σ applied; and with *D* = 2.31e-15 and *n* = 8.11 (see second row of Table 2).

- The ‘Worst-case [durability] (cut-off)’ (grey-dashed line) FCG rate curve is deduced from the automatic ‘Current method with *da/dN* cut-off of 1e-8 m/cycle’ using $\Delta\sqrt{G_{thr}}$ equal to zero and with the $\sqrt{G_{co}}$ $\left(\cong \sqrt{A}\right)$ value with a -3σ; and with *D* = 3.16e-13 and *n* = 5.68 (see third row of Table 2).

The worst-case upper-bound curves using the zero threshold approach shown in Figure 9 calculated via the three different options are significantly different due to the differences in the *D* and *n* values for the two automatic methods compared to the ‘Manual method’. However, as previously noted, the recommended values of *D* and *n* to employ are those obtained using the automatic ‘Current method with all data’. Interestingly, this curve lies to the right of the upper-bound durability rate curves determined by the other two methods. That said, the ‘upper-bound’ curve determined using the ‘cut-off” automatic method is quite similar to that determined using the ‘Current method with all data’ option.

6.4.5 Final comments

Finally, let us consider the behaviour of the fit parameters *D*, *n*, $\Delta\sqrt{G_{thr}}$ and *A*, and the R^2 values, through all iterations for the automatic ‘Current method with all data’ fit which is shown in Figure 10. As discussed in Section 5.2, the numerical behaviour is affected by the choice of the scaling parameter used when calculating the total least squares fit. An additional scale factor of 0.1 has been determined as a suitable value in terms of a trade-off of the run-time against R^2. All results shown for the current method have used this additional scale factor. For a better understanding of the behaviour of the scale factor on a real set of data, the effect of the additional scale parameter on the twenty-five curves for the ‘Current method with all data’ is shown in Figure 11. The general trends of variation as a function of additional scale factor shown in the curves of Figure 11 have been observed by the authors in a variety of data sets, including for metallic materials when fitting to the *K*-form of the Hartman-Schijve equation. The following noteworthy points may be seen in Table 2 and from Figures 8 to 11:

- The iteration progress shown in chart (e) of Figure 10 indicates that the R^2 value varies by a modest amount from about iteration 500 to the final iteration 4438, varying from 0.9623 to 0.9647. Therefore, on a pure R^2 basis, an argument could be made that any fit within that iteration range is equally valid. As can be seen from charts (a) to (d) in Figure 10, that has a consequence for the four fit parameters. For example, at iteration 500 the fit parameters are *D* = 2.82e-12, *n* = 5.22, $\Delta\sqrt{G_{thr}} = 9.11$, $\sqrt{A}$ = 25.85 compared with the final values *D* = 2.31e-15, *n* = 8.11, $\Delta\sqrt{G_{thr}} = 7.14$, $\sqrt{A}$ = 38.73. Since the algorithm ends when *D* and *n* vary by numerically small amounts, the ‘final’ fit is therefore one

value of many numerical similar possibilities (in terms of R^2) which could be altered by changing the final condition for the converged values of *D* and *n*.

- Figure 11 indicates that changing the additional scaling factor used in the solution can influence the final R^2 value and the fit parameters. Figure 11 chart (f) indicates the variation in the number of iterations required as a function of the additional scale factor. Note that the y-axis on this chart is a logarithmic scale. Since the elapsed run-time is directly affected by the number of iterations, charts (e) and (f) help understand how a solution can be obtained by trading the R^2 value against the run-time. The selected additional scale factor of 0.1 is therefore a compromise that produces good R^2 in a reasonable run-time. The elapsed run-times for the cases plotted in Figure 11 vary from around 5 minutes (at a high additional scale factor) to around 12 hours (for a low additional scale factor) using a laptop computer with an 11th Gen Intel Core i9-11950H 2.60GHz processor.

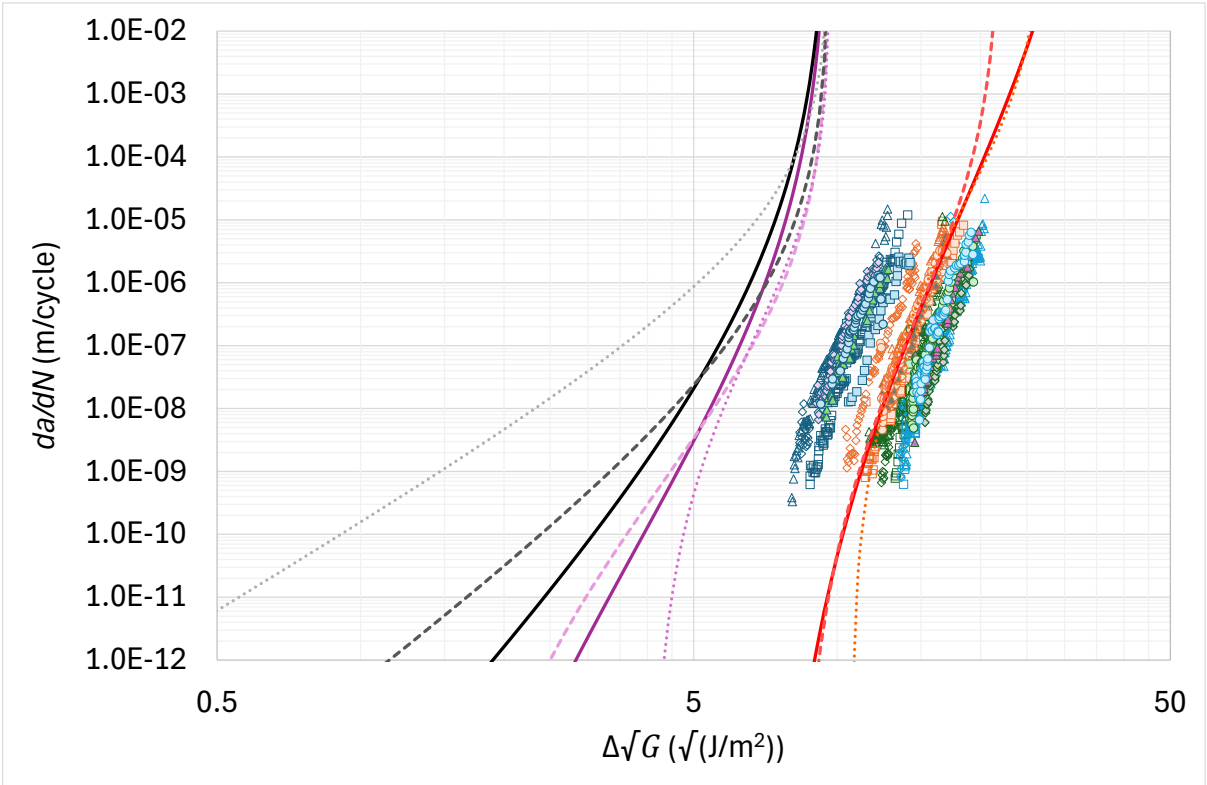


Figure 9. Original data points [14] with the various mean FCG rate curves and worst-case FCG rate curves calculated from the manual and automatic methods. (See text for details of the calculated FCG curves.)

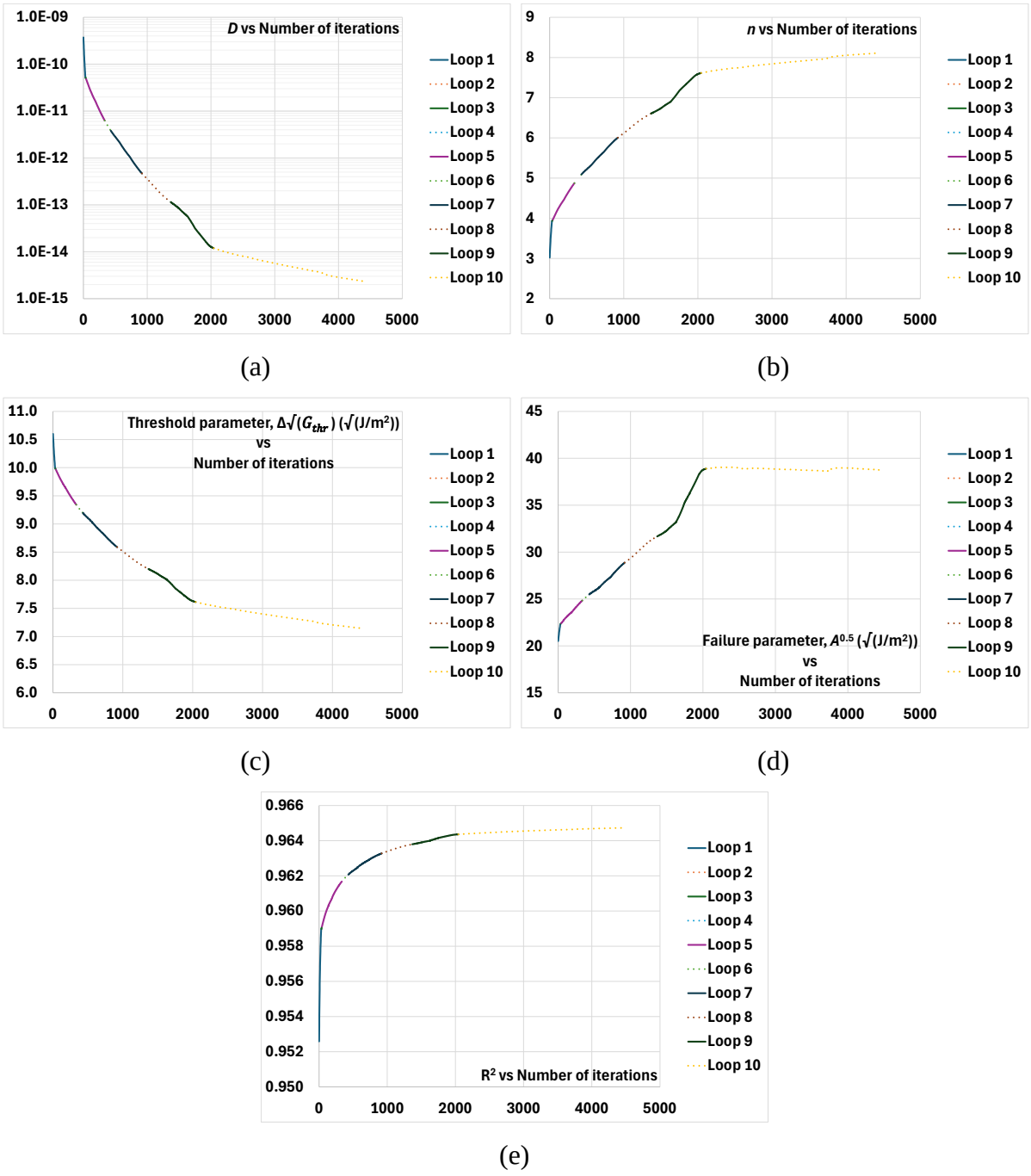


Figure 10. Charts of the through-iteration behaviour of the mean master curve fit parameters and the R^2 of the fit to logarithmic *da/dN* versus logarithmic $\Delta\kappa$ for the data set of 25 curves at $R = 0.1$.

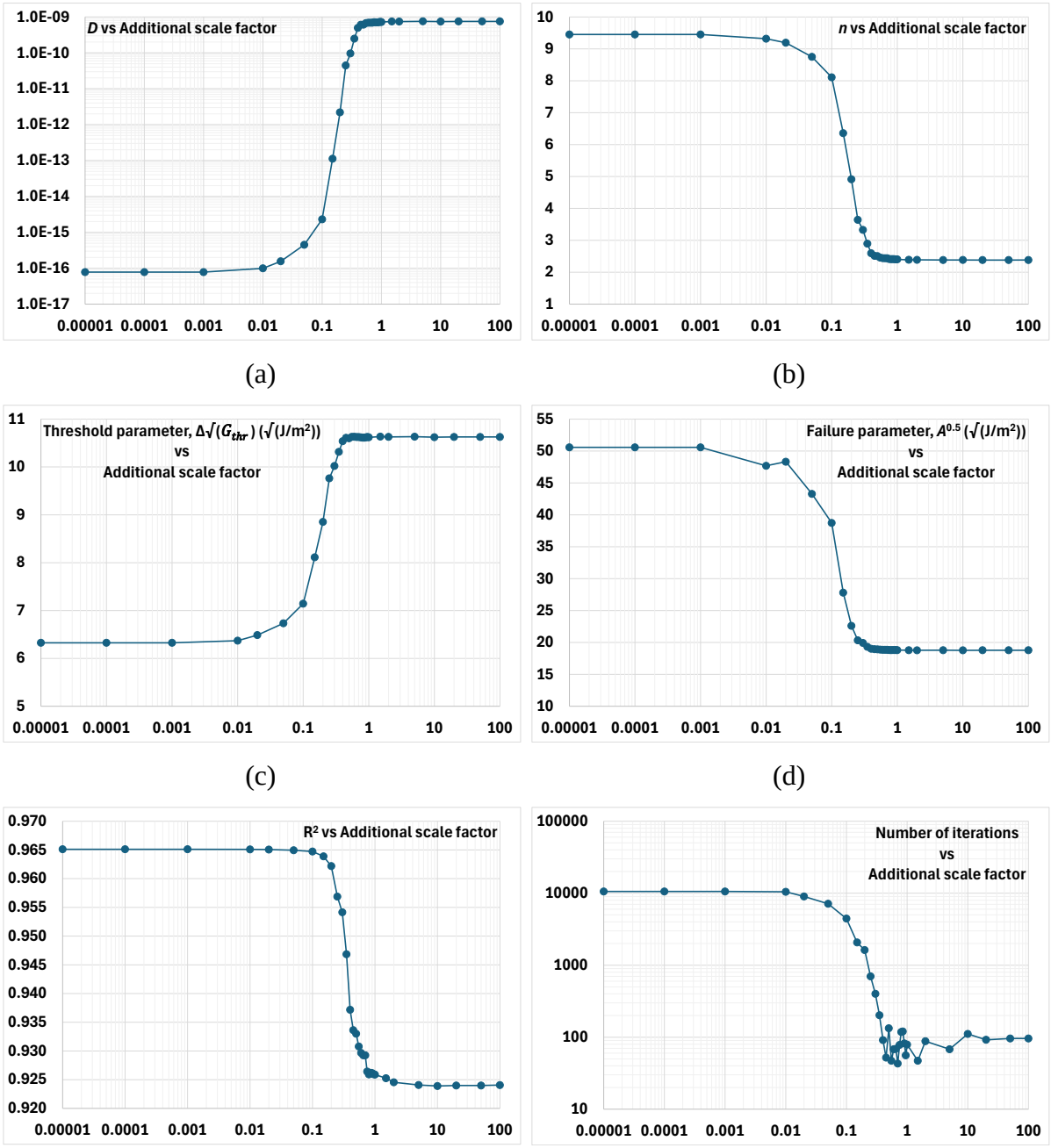


Figure 11. Effect of applying an additional scale factor to the normalisation of the total least squares calculation.

6.5 Multiple curve calculations: application to a data set of one hundred and twenty-six curves with different *R*-ratio values

6.5.1 Introduction

To further test the new automatic methods on a large set of data at different *R*-ratio values, the analyses are now extended from 25 to 126 curves by adding curves at R = 0.3, 0.5 and 0.7. These additional experimental curve sets are described and discussed in [12,15,49-52]. The breakdown of the various curves is shown in Table 3. It should be noted that a manual method fit is not available for comparison with this extended data set due to the difficulty incurred in manipulating such a large data set using the 'Manual method'. The current two automatic calculation methods are therefore able to present a solution which was previously very difficult to obtain.

Table 3. Breakdown of the one hundred and twenty-six curve data set.

R	Number of curves	Number of data points
0.1	25	1927
0.3	18	1573
0.5	75	2828
0.7	8	289
All: 0.1, 0.3, 0.5, 0.7	126	6617

Results of the fitting process using the automatic options of (a) 'Current method with all data' and (b) 'Current method with *da/dN* cut-off of 1e-8 m/cycle' are shown in Table 4. As noted above, there is no alternative manual calculation or reference fit available for comparison to these two automatic methods for this very large data set of 126 FCG rate curves. An example of the master linear Hartman-Schijve plot that is obtained is given in Figure 12 which shows the results from fitting these 126 curves to a graph of logarithmic *da/dN* versus logarithmic $\Delta\kappa$ using the 'Current method with all data' automatic option. A very good master, linear plot is obtained which yields the Hartman-Schijve constants to be D = 7.66e-14, n = 7.11 and $\Delta\sqrt{G_{thr}}$ = 6.11±2.08 ($\sqrt{\mathrm{J/m^2}}$); with R^2 = 0.969.

The various FCG rate curves calculated for R=0.7 from the two automatic methods of interest, using the values of the Hartman-Schjive parameters, i.e. D, n and $\Delta\sqrt{G_{thr}}$, given in Table 4, are shown in Figure 13 along with the experimental results. (The mean G_{co} value used is that reported in [15]: 250 $\mathrm{J/m^2}$ with a standard deviation ±45 $\mathrm{J/m^2}$.) The elapsed run times shown in the final column of Table 4 are obtained using a laptop computer with an 11th Gen Intel Core i9-11950H 2.60GHz processor. The run times are significantly increased compared to the smaller data set for 25 curves shown in Table 2, but nevertheless enable a fit to be achieved within an acceptable timeframe.

6.5.2 The 'Worst-case [mean-2σ]' FCG rate curves

In Figure 13:

- The 'Worst-case [mean-2σ]' FCG rate curve (green-solid line) is deduced from the automatic 'Current method with all data' using the mean $\Delta\sqrt{G_{thr}}$ with a -2σ applied from the individual 126 curve fits and with the mean $\sqrt{G_{co}}$ $\left(\cong\sqrt{A}\right)$ value with a -2σ applied; and with D = 7.66e-14, and n = 7.11 (see first row Table 4 for full details).
- The 'Worst-case [mean-2σ] (cut-off)' (green-dashed line) FCG rate curve is deduced from the automatic 'Current method with *da/dN* cut-off of 1e-8 m/cycle' using the mean $\Delta\sqrt{G_{thr}}$ with a -2σ applied from the individual 126 curve fits and the mean $\sqrt{G_{co}}$ $\left(\cong\sqrt{A}\right)$ value with a -2σ applied; and with D = 5.83e-12 and n = 5.04 (see second row of Table 4 for full details).

As can be seen from Figure 13, that although the constants from the Hartman-Schjive equations from these two automatic options are somewhat different, see Table 4, there is no significant difference between the resulting FCG rate curves. As noted above, although arguments can be made for ignoring data beneath a crack growth rate of 10^{-8} m/cycle, it is generally not the best approach to ignore data. As such the constants determined by the

automatic calculations using the 'Current method with all data' should be considered to be the better option, noting as before a slightly higher R^2 value compared to the 'cut-off' automatic method.

6.5.3 The 'Worst-case [durability]' FCG curves

The worst-case [durability] FCG rate curves shown in Figure 13 use a value of zero for $\Delta\sqrt{G_{thr}}$ and the mean $\sqrt{G_{co}}$ $\left(\cong\sqrt{A}\right)$ value with a -3σ standard deviation, and the values of *D* and *n* as shown in Table 4 for the two automatic methods. At rates above about 1e-7 m/cycle the two automatic methods give very similar FCG rate curves. Below about 1e-7 m/cycle the 'Worst-case [durability] (cut-off)' curve is a somewhat less conservative curve, although the differences are relatively small. For the reasons stated above, it is considered that the Hartman-Schjive constants determined by the automatic calculations using the 'Current method with all data' should be considered to be the better option.

Table 4. The values of the Hartman-Schijve parameters and R^2 resulting from the two automatic calculation methods from fitting of the one hundred and twenty-six tests at various *R*-ratios for the CFRP.

Method	*D*	*n*	$\Delta\sqrt{G_{thr}}$ and std. dev. $(\sqrt{\mathrm{J/m^2}})$	$\sqrt{A}$ and std. dev. $(\sqrt{\mathrm{J/m^2}})$	R^2	Elapsed run times (s)
Current method with all data	7.66e-14	7.11	6.11±2.08	30.24±12.28	0.969	118450
Current method with *da/dN* cut-off of 1e-8	5.83e-12	5.04	6.96±2.33	24.03±6.49	0.958	28265

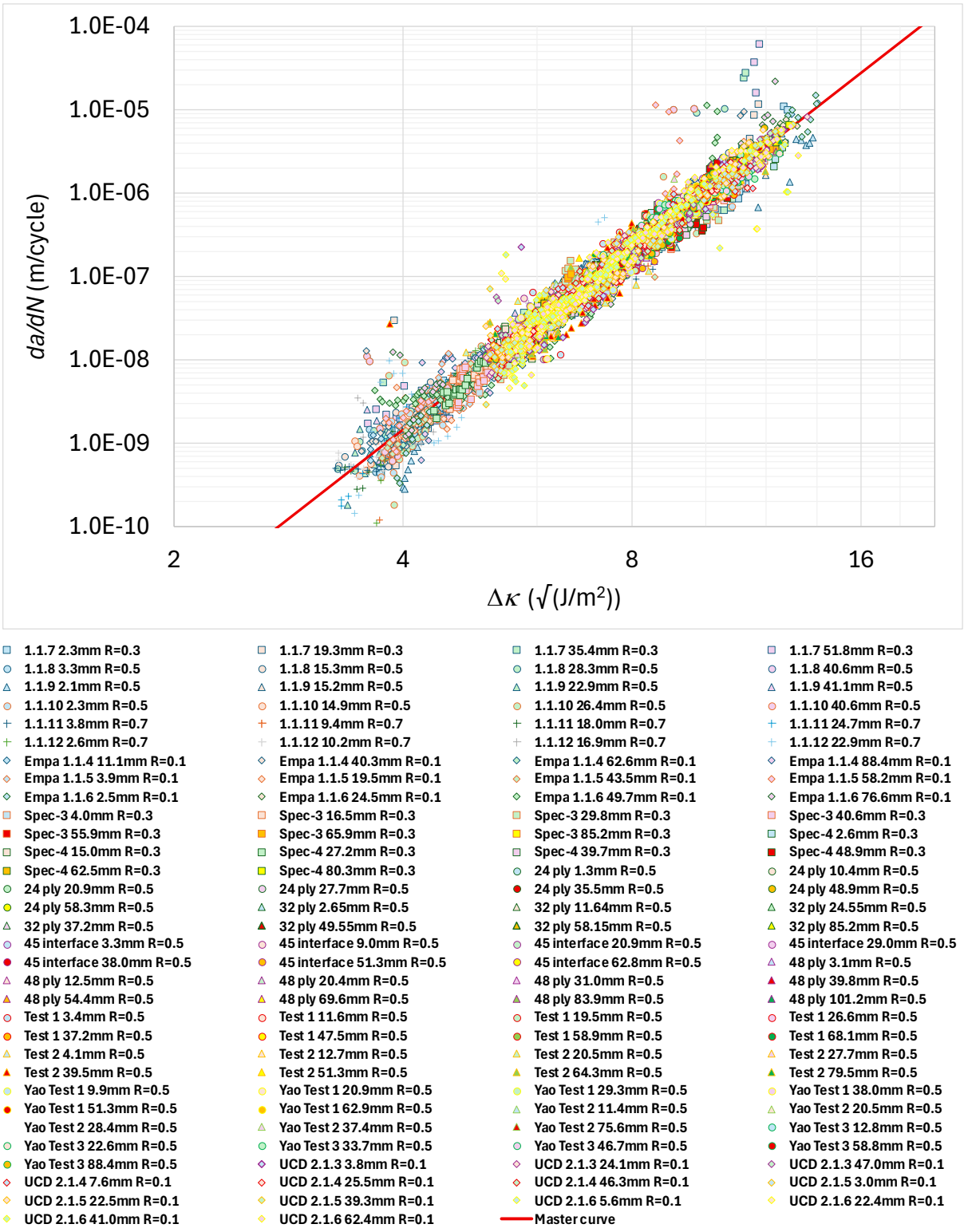


Figure 12. Logarithmic *da/dN* versus logarithmic $\Delta\kappa$ for the one hundred and twenty-six sets of experimental data [12,14,15,49-52] at various *R*-ratios of 0.1, 0.3, 0.5 and 0.7. Fit data shown is using the 'Current method with all data' results to obtain the master, linear Hartman-Schijve plot and the Hartman-Schijve constants are found to be: D = 7.66e-14, n = 7.11 and $\Delta\sqrt{G_{thr}}$ = 6.11±2.08 ($\sqrt{\text{J/m}^2}$); with R^2 = 0.969.

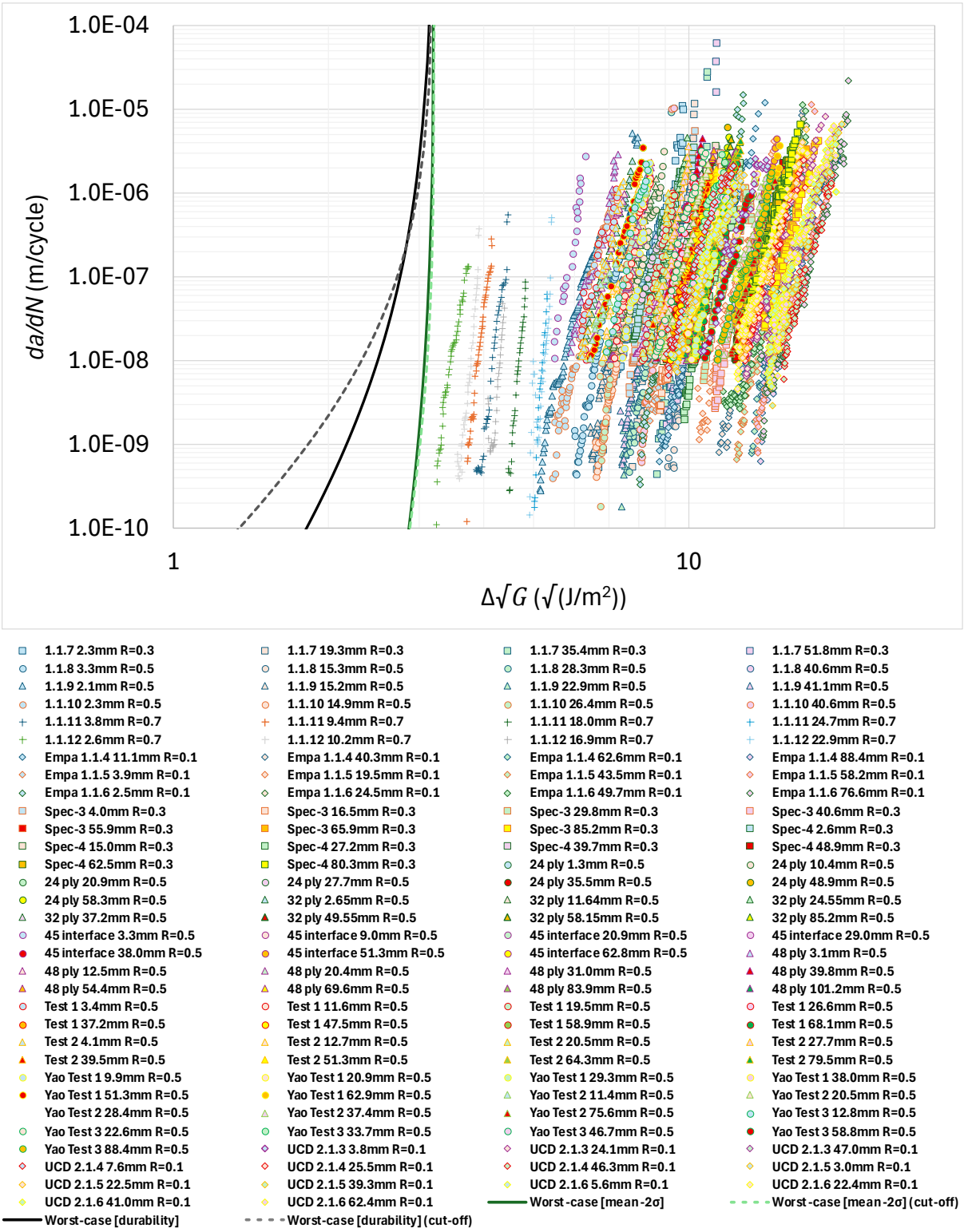


Figure 13. Original data points [15] with the mean FCG rate curves and worst-case (durability) FCG rate curves (for R=0.7) for the one hundred and twenty-six sets of experimental data [12,14,15,49-52] calculated from the 'Current method with all data' and the 'Current method with a *da/dN* cut-off of 1e-8 m/cycle' automatic options. (See text for details of the calculated FCG rate curves.)

7. Conclusions

The Hartman-Schijve methodology offers a direct route to calculating various fatigue crack growth (FCG) rate curves that are associated with delaminations growing in fibre polymer-matrix composites. However, up to the present, only an essentially 'manual' method has been described to implement this Hartman-Schijve method. This is a difficult and tedious implementation route, especially if the operator is inexperienced. Further, for very large data sets there is great difficulty incurred when manipulating such a large amount of data using the 'Manual method'. Therefore, the main aim of the present paper has been to introduce a novel computer model, and the associated software, namely 'Zencrack : Material Curve Fitting Utility' from Zentech International Limited, UK, to obtain automatically the Hartman-Schijve constants and hence deduce the 'worst-case upper-bound' FCG rate curve for small, naturally-occurring, delaminations.

To achieve such an 'automatic' method, current work has taken previous published algorithms that employ a total least squares method for the fitting process of the experimental input data and has investigated the effect of a normalising scaling factor that is an essential feature of the algorithm. Additional iteration controls have been added to improve the efficiency of the overall procedure, allowing very large data sets to be fitted within reasonable elapsed run-times. Investigation of the numerical process, and comparisons with previous manual fitting results, has indicated that, from the perspective of the R^2 master-curve fit, there is not a unique solution but instead a range of numerical solutions that can provide near-equivalent R^2 results. This pure numerical, automatic approach lacks the application of the 'engineering knowledge' that has been used in previous manual fitting methods when used to study crack growth in metals. However, the computational algorithm allows additional constraint to be defined on the threshold and failure values of the FCG curves, for example, by forcing the same failure constants onto a group of FCG rate curves. Further, the efficient nature of the solution allows fits to be generated for large data sets more quickly than with manual methods and, indeed, can handle large data sets that cannot be analysed using the manual method. It has been found that an automatic calculation method that includes all the input data gives overall the most reproducible and accurate values of the Hartman-Schijve constants and is the recommended approach. Once these Hartman-Schijve constants have been ascertained the 'worst-case upper-bound' FCG rate curve for small, naturally-occurring, delaminations may be readily calculated. Such a FCG rate curve may now be employed for developing, characterising and comparing different composite materials, and for designing and lifing in-service aircraft components and structures.

CRediT author statement
Ramesh Chandwani: Review & Editing. **Chris Timbrell**: Analysis and Methodology, Writing, Review & Editing. **Bamber Blackman**: 'Writing, Review and Editing'. **Rhys Jones**: Analysis and Methodology, Review & Editing **Anthony J. Kinloch**: Validation, Writing, Review & Editing.

Declaration of competing interest
The authors declare that they have no known competing financial interests or personal relationships that could have appeared to influence the work reported in this paper.

Data availability
Data will be made available on request albeit at the end of the ESIS Round Robin.

Funding: This work did not receive external funding.

REFERENCES

1. ISO Standard, 15024. Fibre-reinforced plastic composites - Determination of mode I interlaminar fracture toughness, G_{Ic}, for unidirectionally reinforced materials. International Standards Organisation. 2001, Geneva, Switzerland.
2. Federal Aviation Authority, (2009) Airworthiness Advisory Circular No: 20-107B. Composite Aircraft Structure, 09/08/2009. Available online at: https://www.faa.gov/regulations_policies/advisory_circulars/index.cfm/go/document.information/documentID/99693 (accessed on 07/06/2025).
3. Transportation Safety Board of Canada. Loss of Rudder in Flight Air Transat Airbus A310-308 C-GPAT, Miami, Florida, 90 nm S, 6 March 2005. Report Number A05F0047. Available online at: https://www.tsb.gc.ca/eng/rapports-reports/aviation/2005/a05f0047/a05f0047.html (accessed on 19/12/2023).
4. Mueller E.M., Starnes S., Strickland N., Kenny P., William C., The detection, inspection, and failure analysis of a composite wing skin defect on a tactical aircraft. Composite Structures, 2016, 145, 186-193.
5. Department of Defense Joint Service Specification Guide, Aircraft Structures, JSSG-2006, originally dated October 1998.
6. MIL-STD-1530D. Department of Defense Standard Practice, Washington, DC, USA, 2016. Available online at: http://everyspec.com/MIL-STD/MIL-STD-1500-1599/MIL-STD-1530D_55392/#:~:text=%2DAUG%2D2016)-,MIL%2DSTD%2D1530D%2C%20DEPARTMENT%20OF%20DEFENSE%20STANDARD%20PRACTICE%3A,while%20managing%20cost%20and%20schedule (accessed on 05/12/2023).
7. NASA-HDBK-5010. Fracture Control Handbook for Payloads, Experiments, and Similar Hardware. May 2005, Revalidated 2012. Available online at: https://standards.nasa.gov/standard/nasa/nasa-hdbk-5010 (accessed on 26/12/2023).
8. Rans C., Alderliesten R.C., Benedictus R., Misinterpreting the results: How similitude can improve our understanding of fatigue delamination growth. Composites Science Technology, 2011, 71, 230-238.
9. Yao L., Alderliesten R.C., Zhao M., Benedictus R., Bridging effect on Mode I fatigue delamination behavior in composite laminates. Composites A, 2014, 63, 103-109.
10. Simon I., Banks-Sills L., Fourman V., Mode I delamination propagation and R-ratio effects in woven DCB specimens for a multi-directional layup. International Journal Fatigue, 2017, 96, 237-251.
11. Jones R., Kinloch A.J., Michopoulos J.G., Brunner A.J., Phan N., Delamination growth in polymer-matrix fibre composites and the use of fracture mechanics data for material characterisation and life prediction. Composite Structures, 2017,180, 316-333.
12. Yao L., Alderliesten R.C., Jones R., Kinloch A.J., Delamination fatigue growth in polymer-matrix fibre composites: a methodology for determining the design and lifing allowables. Composite Structures, 2018, 196, 8-20.
13. Jones R., Kinloch A.J., A way forward for industry to determine valid cyclic-fatigue relationships for polymer-matrix fibre composites. Procedia Structural Integrity, 2020, 28, 26-38.
14. Michel S., Murphy N., Kinloch A.J., Jones R., On cyclic-fatigue crack growth in carbon-fibre-reinforced epoxy-polymer composites. Polymers, 2024, 16, 435.

15. Michel S., Kinloch A.J., Jones R., Cyclic fatigue crack growth in polymer composites: Data interpretation via the Hartman-Schijve methodology. Engineering Fracture Mechanics, 2025, 314, 110743.

16. United States Air Force. Durability and Damage Tolerance Certification for Additive Manufacturing of Aircraft Structural Metallic Parts, Structures Bulletin EZ-SB-19-01, Wright Patterson Air Force Base: Dayton, OH, USA, June 2019. Available online at: https://www.daytonaero.com/_files/ugd/742fa6_f655412ea39b4ab89e7fa86686e6e8f6.pdf (accessed on 07/06/2025).

17. Hartman A., Schijve J., The effects of environment and load frequency on the crack propagation law for macro FCG in aluminium alloys. Engineering Fracture Mechanics, 1970, 1, 615-631.

18. Iliopoulos A., Michopoulos J.G., R. Jones R., Kinloch A.J., Peng D., A framework for automating the parameter determination of crack growth models. International Journal Fatigue, 2023, 169, 107490.

19. Russo A., Riccio A., Palumbo C., Sellitto A., Fatigue driven delamination in composite structures: Definition and assessment of a novel fracture mechanics based computational tool. International Journal Fatigue, 2023, 166, 107257.

20. Russo A., Palumbo C., Sellitto A., Riccio A., The peculiar SMart-Time XB approach for delamination growth prediction and its evolution towards fatigue investigations. International Journal Solids Structures, 2024, 291, 112681.

21. ASTM E647-23b, Measurement of fatigue crack growth rates. ASTM. 2023, West Conshohocken, PA, USA.

22. Paris P.C., Gomez R.E., Anderson W.E., A rational analytic theory of fatigue. The Trend in Engineering, 1961, 13/1, 9-14.

23. Paris P.C., Erdogan F., Critical analysis of crack growth propagation laws. ASME Transactions Journal Basic Engineering, 1963, 85D, 528-534.

24. Paris P.C., A brief history of the crack tip stress intensity factor and its application. Meccanica, 49, 2014, 759–764.

25. Jones R., Kovarik O., Bagherifard S., Cizek J., Lang J., Damage tolerance assessment of AM 304L and cold spray fabricated 316L steels and its implications for attritable aircraft. Engineering Fracture Mechanics, 2021, 254, 107916.

26. Castro J.T.P., Meggiolaro M.A. Miranda A.C.O, A Note on Fatigue Crack Growth Predictions Based on Damage Accumulation Ahead of the Crack Tip. Mechanics of Solids in Brazil, 2007, M. Alves and H.S. da Costa Mattos (Eds.), Brazilian Society of Mechanical Sciences and Engineering.

27. Brunner A.J., Quantification of delamination resistance data of FRP composites and its limits. Proc. I. Mech. Eng. Part L: Journal of Materials: Design and Applications, 2024, 239, 694-705.

28. Brunner A.J., Scatter, scope and structures: What fatigue fracture testing of fiber polymer composites is all about. IOP Conference Series: Materials Science Engineering, 2018, 388, 012003.

29. Jones R., Hu W., Kinloch A.J., A convenient way to represent fatigue crack growth in structural adhesives. Fatigue Fracture Eng. Mater. Structures, 2014, 38, 379-391.

30. Jones R., Kinloch A.J., Hu W., Cyclic-fatigue crack growth in composite and adhesively-bonded structures: The FAA slow crack growth approach to certification and the problem of similitude. International Journal Fatigue, 2016, 88, 10-18.

31. Jones R., Kinloch A.J., Ang A.S.M., Modelling fatigue crack growth in high-density polyethylene and acrylonitrile butadiene styrene polymers. Polymers, 2024, 16, 1299.

32. Jones R., Pitt S., Brunner A.J., Hui D., Fatigue crack growth in nano-composites. Composite Structures, 2013, 99, 75-379.

33. Kinloch A.J., Jones R., Michopoulos J.G., Fatigue crack growth in epoxy polymer nanocomposites. Philos. Trans. Royal Society, 2020, A379, 20200436.

34. Ye J., Syed A.K., Zhang X., Eimer E., Williams S., Fatigue crack growth behaviour in an aluminium alloy Al-Mg-0.3Sc produced by wire based directed energy deposition process. Fatigue Fracture Eng. Mater. Struct., 2023, 46, 3927-2938.

35. Kovarik O., Cizek J., Klecka, J., Fatigue crack growth rate description of RF-plasma-sprayed refractory metals and alloys. Materials, 2023, 16, 1713.

36. Dastgerdi J.N., Jaberi O., Remes H., Lehto P., Toudeshky H.H., Kuva J., Fatigue damage process of additively manufactured 316L steel using X-ray computed tomography imaging. Additive Manufacturing, 2023, 70, 103559.

37. Jones R., Ang A., Peng D., Champagne V.K., Michelson A., Birt A., Modelling crack growth in additively manufactured Inconel 718 and Inconel 625. Metals, 2023, 13, 300.

38. Peng D., Jones R., Ang A.S.M., Michelson A., Champagne V., Birt A., Pinches S., Kundu S., Alankar A., Singh Raman RK. Computing the durability of WAAM 18Ni 250 maraging steel specimens. Fatigue Fracture Eng. Mater. Struct. 2022, 45, 3535-3545.

39. Jones R., Rans C., Iliopoulos A.P., Michopoulos J.G., Phan N., Peng D., Modelling the variability and the anisotropic behaviour of crack growth in SLM Ti-6Al-4V. Materials, 2021, 14, 1400.

40. Iliopoulos A.P., Jones R., Michopoulos J.G., Phan N., Rans C., Further studies into crack growth in additively manufactured materials. Materials, 2020, 13, 2223.

41. Jones R., Ang A., Aston, R.W., Schoenborn N.D., Champagne V.K., Peng D., Phan N.D., On the growth of small cracks in 2024- T3 and Boeing Space, Intelligence and Weapon Systems AM LPBF Scalmalloy®. Fatigue Fracture Eng. Mater. Struct., 2024, 38, 41-33.

42. Chan S., Peng D., Ang A.S.M., Nicholas M.B., Champagne V.K., Birt A., Michelson A., Langan S., Watts J., Jones R., Further studies into the growth of small naturally occurring three-dimensional cracks in additively manufactured and conventionally built materials. Crystals, 2025, 15, 544.

43. Main B., Evans R., Walker K., Yu X., Molent L., Lessons from a fatigue prediction challenge for an aircraft wing shear tie post. International Journal Fatigue, 2019, 123, 53-65.

44. Tan J., Chen B., Coalescence and growth of two coplanar short cracks in AA7050-T7451 aluminium alloys. Engineering Fracture Mechanics, 2013, 102, 324-333.

45. Tan J., Chen B. A new fracture area method for predicting the growth of a newly coalesced crack in AA7050-T7451 aluminium alloy. Theor. Appl. Fracture Mech., 2015, 75, 146-150.

46. Niu M.C.Y., Composite Airframe Structures: Practical Design Information and Data, Conmilit Press, Hong Kong, 1992.

47. Rouchon J., Fatigue and Damage Tolerance Evaluation of Structures: The Composite Materials Response. 22nd Plantema Memorial Lecture, 25th ICAF Symposium,

Hamburg, Germany, Rotterdam, The Netherlands, National Aerospace Laboratory NLR, NLR-TP-2009-221, 2009.

48. Iliopoulos A., Michopoulos J.G., CGROW v0.9.0: A framework for fatigue crack growth model parameter determination. U.S. Naval Research Laboratory, 24 Sep 2021. Available online at: https://github.com/USNavalResearchLaboratory/cgrow (accessed 4/7/2024).
49. Yao L., Sun Y., Alderliesten R.C., Benedictus R., Zhao M., Fibre bridging effect on the Paris relation for mode I fatigue delamination growth in composites with consideration of interface configuration. Composite Structures, 2017, 159, 471-478.
50. Yao L., Sun Y., Zhao M., Alderliesten R.C., Benedictus R., Stress ratio dependence of fibre bridging significance in mode I fatigue delamination growth of composite laminates. Composites A, 2017, 95, 65-74.
51. Yao L., Sun Y., Guo L., Alderliesten R.C., Benedictus R., Zhao M., Jia, L., Fibre bridging effect on the Paris relation on mode I fatigue delamination in composite laminates with different thicknesses. International Journal Fatigue, 2017, 103, 196-206.
52. Yao L., Chuai M., Lyu Z., Chen X., Guo L., Alderliesten R.C., A proposal for similitude in characterizing fatigue delamination behavior with fibre bridging of carbon-fibre reinforced polymer composites. Engineering Fracture Mechanics, 2024, 295, 109756.